

Measurement of the CKM angle γ using $B_s^0 \rightarrow D_s K \pi\pi$ decays

P. d'Argent¹, E. Gersabeck², M. Kecke¹, M. Schiller³

¹*Physikalisches Institut, Ruprecht-Karls-Universität Heidelberg, Heidelberg, Germany*

²*School of Physics and Astronomy, University of Manchester, Manchester, United Kingdom*

³*School of Physics and Astronomy, University of Glasgow, Glasgow, United Kingdom*

Abstract

We present the first measurement of the weak phase $2\beta + \gamma$ obtained from a time-dependent (amplitude) analysis of $B_s^0 \rightarrow D_s K \pi\pi$ decays using proton-proton collision data corresponding to an integrated luminosity of **xxx** fb⁻¹ recorded by the LHCb detector.

Contents

1	Introduction	1
2	Sensitivity studies	2
2.1	PDF	2
2.2	Estimation of coherence factor	3
2.3	Results	5
3	Selection	8
3.1	Cut-based selection	8
3.2	Multivariate stage	9
4	Fits to invariant mass distributions of signal and normalization channel	14
4.1	Signal models for $m(D_s\pi\pi\pi)$ and $m(D_sK\pi\pi)$	14
4.2	Background models for $m(D_s\pi\pi\pi)$	15
4.3	Background models for $m(D_sK\pi\pi)$	15
4.4	Fit to $B_s^0 \rightarrow D_s\pi\pi\pi$ candidates	17
4.5	Fit to $B_s^0 \rightarrow D_sK\pi\pi$ candidates	17
4.6	Extraction of signal weights	17
5	Flavour Tagging	19
5.1	OS tagging calibration	20
5.2	SS tagging calibration	20
5.3	Tagging performance comparison between the signal and normalization channel	20
5.4	Combination of OS and SS taggers	21
6	Decay-time acceptance	24
6.1	Comparison of acceptance in subsamples	25
6.2	Results	27
7	Decay-time Resolution	32
7.1	Formalism	32
7.2	Decay-time Error in Run I & Run II	32
7.3	Fits to the decay time distributions	33
7.4	Results	34
8	Time dependent fit	36
8.1	sFit to $B_s^0 \rightarrow D_s\pi\pi\pi$ data	36
8.2	sFit to $B_s^0 \rightarrow D_sK\pi\pi$ data	36
8.3	Results	36
A	Detailed mass fits	37
B	Decay-time Resolution fits	41
C	MC corrections	42

D Data distributions	47
D.1 Comparison of signal and calibration channel	47
D.2 Comparison of Run-I and Run-II data	49
D.3 Comparison of D_s final states	51
D.4 Comparison of trigger categories	53
References	55

1 Introduction

- The weak phase γ is the least well known angle of the CKM unitary triangle. A key channel to measure γ is the time-dependent analysis of $B_s^0 \rightarrow D_s K$ decays [1], [2].
 The $B_s^0 \rightarrow D_s K\pi\pi$ proceeds at tree level via the transitions shown in Fig. 1.1 a) and b).

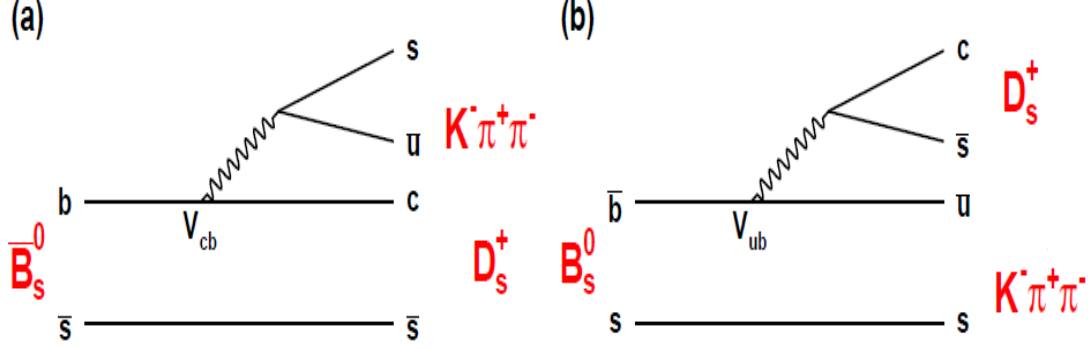


Figure 1.1: Feynman diagram of the $B_s^0 \rightarrow D_s K\pi\pi$ decay, proceeding via a) $b \rightarrow c$ transitions or b) $b \rightarrow u$ transitions.

To measure the weak CKM phase $\gamma \equiv \arg[-(V_{ud}V_{ub}^*)/(V_{cd}V_{cb}^*)]$, a decay with interference between $b \rightarrow c$ and $b \rightarrow u$ transitions at tree level is needed [1]. As illustrated in Fig. 1.1, this is the case for the presented decay mode. A measurement of γ using $B_s^0 \rightarrow D_s K\pi\pi$ decays, where the $K\pi\pi$ subsystem is dominated by excited kaon states such as the $K_1(1270)$ and $K_1(1400)$ resonances, will succeed the branching ratio measurement presented in this note. It is complementary to the above mentioned analysis of $B_s^0 \rightarrow D_s K$, making use of a fully charged final state, where every track is detected in the vertex locator. To account for the non-constant strong phase across the Dalitz plot, one can either develop a time-dependent amplitude model or select a suitable phase-space region and introduce a coherence factor as additional hadronic parameter to the fit.
 This analysis is based on the first observation of the $B_s^0 \rightarrow D_s K\pi\pi$ decay presented in [3] and [4], where its branching ratio is measured relative to $B_s^0 \rightarrow D_s \pi\pi\pi$. The result obtained by the previous analysis is $0.052 \pm 0.005 \pm 0.003$, where the uncertainties are statistical and systematical, respectively. The branching ratio measurement is updated, exploiting the full Run 1 data sample, corresponding to 3 fb^{-1} of integrated luminosity.

2 Sensitivity studies

2.1 PDF

First, I define the purely hadronic amplitudes for a given phasespace point x . The weak phase dependence is written latter explicitly in the pdf.

$$A(B_s^0 \rightarrow D_s^- K^+ \pi\pi) \equiv A(x) = \sum_i a_i A_i(x) \quad (2.1)$$

$$A(B_s^0 \rightarrow D_s^+ K^- \pi\pi) \equiv \bar{A}(\bar{x}) = \sum_i \bar{a}_i \bar{A}_i(\bar{x}) \quad (2.2)$$

$$A(\bar{B}_s^0 \rightarrow D_s^- K^+ \pi\pi) = \bar{A}(x) \text{ (Assuming no direct CPV)} \quad (2.3)$$

$$A(\bar{B}_s^0 \rightarrow D_s^+ K^- \pi\pi) = A(\bar{x}) \text{ (Assuming no direct CPV)} \quad (2.4)$$

The full time-dependent amplitude pdf is given by:

$$\begin{aligned} P(x, t, q_t, q_f) \propto & [(|A(x)|^2 + |\bar{A}(x)|^2) \cosh\left(\frac{\Delta\Gamma t}{2}\right) \\ & + q_t q_f (|A(x)|^2 - |\bar{A}(x)|^2) \cos(m_s t) \\ & - 2\text{Re}(A(x)^* \bar{A}(x) e^{-iq_f(\gamma-2\beta_s)}) \sinh\left(\frac{\Delta\Gamma t}{2}\right) \\ & - 2q_t q_f \text{Im}(A(x)^* \bar{A}(x) e^{-iq_f(\gamma-2\beta_s)}) \sin(m_s t)] e^{-\Gamma t} \end{aligned} \quad (2.5)$$

where $q_t = +1$ (-1) for a B_s^0 (\bar{B}_s^0) tag and $q_f = +1$ (-1) for $D_s^- K^+ \pi\pi$ ($D_s^+ K^- \pi\pi$) final states.

Integrating over the phasespace, we get

$$\begin{aligned} \int P(x, t, q_t, q_f) dx \propto & [\cosh\left(\frac{\Delta\Gamma t}{2}\right) \\ & + q_t q_f \left(\frac{1-r^2}{1+r^2}\right) \cos(m_s t) \\ & - 2 \left(\frac{\kappa r \cos(\delta - q_f(\gamma - 2\beta_s))}{1+r^2}\right) \sinh\left(\frac{\Delta\Gamma t}{2}\right) \\ & - 2q_t q_f \left(\frac{\kappa r \sin(\delta - q_f(\gamma - 2\beta_s))}{1+r^2}\right) \sin(m_s t)] e^{-\Gamma t} \\ = & [\cosh\left(\frac{\Delta\Gamma t}{2}\right) + q_t q_f C \cos(m_s t) - \kappa D_{q_f} \sinh\left(\frac{\Delta\Gamma t}{2}\right) - q_t \kappa S_{q_f} \sin(m_s t)] e^{-\Gamma t} \end{aligned} \quad (2.6)$$

where the C, D_{q_f}, S_{q_f} are defined exactly as for $D_s K$. The coherence factor is defined as :

$$\kappa e^{i\delta} \equiv \frac{\int A(x)^* \bar{A}(x) dx}{\sqrt{\int |A(x)|^2 dx} \sqrt{\int |\bar{A}(x)|^2 dx}} \quad (2.7)$$

$$r \equiv \frac{\sqrt{\int |\bar{A}(x)|^2 dx}}{\sqrt{\int |A(x)|^2 dx}} \quad (2.8)$$

30 and appears in front of the D_{qf}, S_{qf} terms. This means one additional fit parameter for
 31 the lifetime fit. In the limit of only one contributing resonance $\kappa \rightarrow 1$.

32

33 2.2 Estimation of coherence factor

34 To estimate the coherence factor we could generate many toys with random a_i and \bar{a}_i
 35 values (see https://twiki.cern.ch/twiki/pub/LHCbPhysics/Bu2DKstar/LHCb-ANA-2017-005_v1.pdf) using the set of amplitudes show in our last talk. However with so many
 36 interfering amplitudes, I would be surprised if you couldn't generate every possible value
 37 for κ . In any case, this would give us a range where to expect possible values for κ . Worst
 38 case would be $0 \leq \kappa \leq 1$.

39

40 Assumptions:

41

- $A(x) = \sum_i a_i A_i(x)$

42

$$\bar{A}(x) = \sum_i \bar{a}_i \bar{A}_i(x)$$

43

- Use amplitudes from flavor-averaged, time-integrated fit

44

- Draw random a_i and \bar{a}_i values

45

- Constraints:

46

$$\int(|a_i A_i(x)|^2 + |\bar{a}_i \bar{A}_i(x)|^2) dx/N = F_i^{eff}$$

47

$$r \approx 0.4$$
 (ration of CKM elements)

48

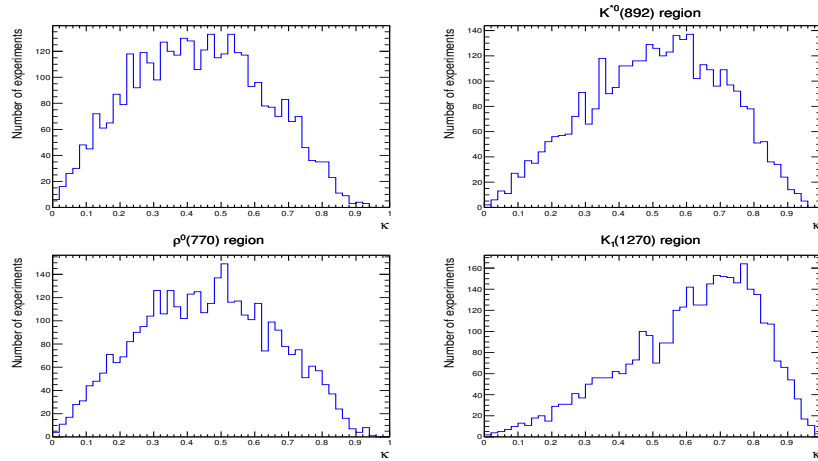


Figure 2.1

Table 2.1

Region	$<\kappa>$ (%)	Cut eff. (%)
Full	43	100
$K^*(892)$	51	43
$\rho^0(770)$	46	47
$K_1(1270)$	61	23

49 2.3 Results

50 Assumptions:

- 51 • Use amplitudes from flavor-averaged, time-integrated fit
- 52 • $r = 0.4$ (ratio of CKM elements)
- 53 • PDG values for: $\tau, \Delta m_s, \Delta\Gamma, \beta_s$
- 54 • $\epsilon(x, t) = \text{const.}$, perfect resolution
- 55 • $\epsilon_{Tag} = 0.66, \langle \omega \rangle = 0.4$
- 56 • $N_{signal} = 3000$ (Run1+15/16 data)

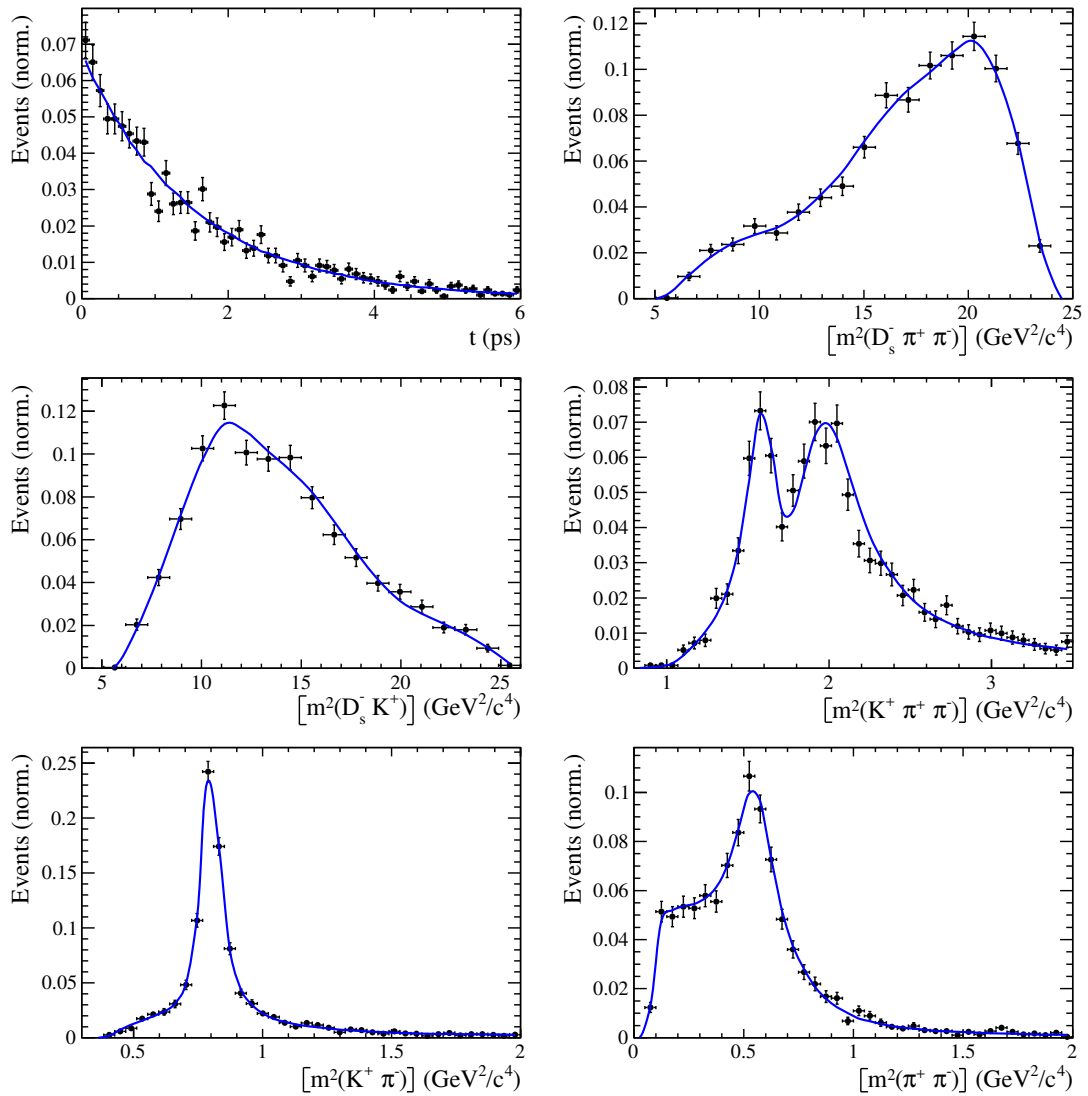
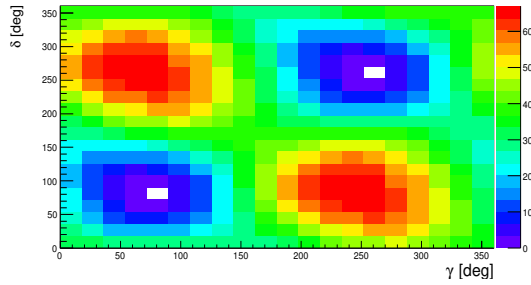


Figure 2.2: Example toy fit



Generated values:

$$\gamma = 70^\circ, \delta = 100^\circ$$

Fit result:

$$\begin{aligned} \gamma &= 74 \pm 15^\circ, \delta = 84 \pm 15^\circ \\ (\gamma &= 254 \pm 15^\circ, \delta = 264 \pm 15^\circ) \end{aligned}$$

Figure 2.3: Likelihood scan

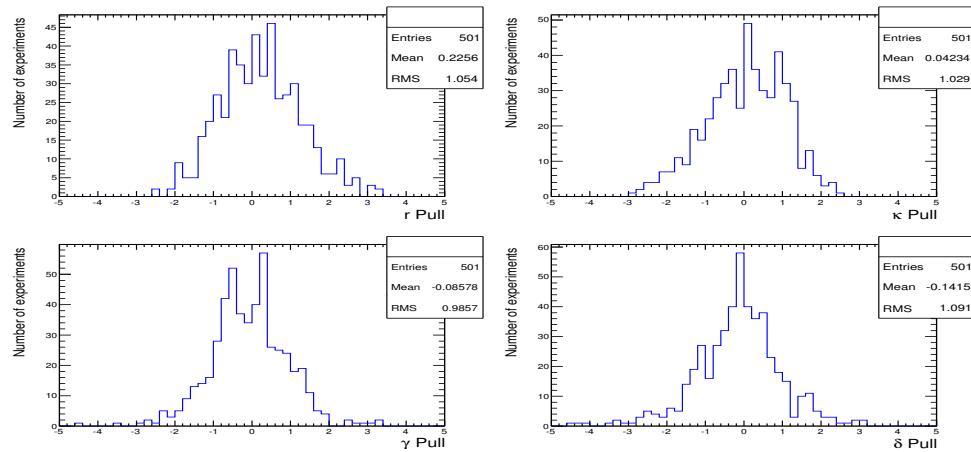


Figure 2.4: Pulls

Table 2.2

	Generated	Full PDF	Phasespace integrated
r	0.4	0.38 ± 0.06	unstable
κ	0.2	0.23 ± 0.13	0.2 (fixed)
δ	100	99 ± 22	unstable
γ	70	70 ± 17	unstable

	Generated	Full PDF	Phasespace integrated
r	0.4	0.44 ± 0.07	0.43 ± 0.11
κ	0.4	0.41 ± 0.14	0.4 (fixed)
δ	100	101 ± 19	95 ± 41
γ	70	69 ± 16	66 ± 40

	Generated	Full PDF	Phasespace integrated
r	0.4	0.41 ± 0.08	0.39 ± 0.11
κ	0.6	0.60 ± 0.13	0.6 (fixed)
δ	100	98 ± 17	92 ± 25
γ	70	68 ± 17	65 ± 28

	Generated	Full PDF	Phasespace integrated
r	0.4	0.42 ± 0.09	0.39 ± 0.09
κ	1.0	0.96 ± 0.03	1.0 (fixed)
δ	100	100 ± 17	100 ± 17
γ	70	66 ± 17	67 ± 17

57 **3 Selection**

58 For the presented analysis, we reconstruct the $B_s^0 \rightarrow D_s K\pi\pi$ decay through two different
 59 final states of the D_s meson, $D_s \rightarrow KK\pi$ and $D_s \rightarrow \pi\pi\pi$. Of those two final states
 60 $D_s \rightarrow KK\pi$ is the most prominent one, while $\mathcal{BR}(D_s \rightarrow \pi\pi\pi) \approx 0.2 \cdot \mathcal{BR}(D_s \rightarrow KK\pi)$
 61 holds for the other one.

62 A two-fold approach is used to isolate the $B_s^0 \rightarrow D_s K\pi\pi$ candidates from data passing
 63 the stripping line. First, further one-dimensional cuts are applied to reduce the level of
 64 combinatorial background and to veto some specific physical background. This stage is
 65 specific to the respective final state in which the D_s meson is reconstructed, since different
 66 physical backgrounds, depending on the respective final state, have to be taken into
 67 account. After that, a multivariate classifier is trained which combines the information
 68 of several input variables, including their correlation, into one powerful discriminator
 69 between signal and combinatorial background. For this stage, all possible D_s final states
 70 are treated equally.

71 **3.1 Cut-based selection**

72 In order to minimize the contribution of combinatorial background to our samples, we
 73 apply the following cuts to the b hadron:

- 74 • DIRA > 0.99994
- 75 • min IP $\chi^2 < 20$ to any PV,
- 76 • FD $\chi^2 > 100$ to any PV,
- 77 • Vertex $\chi^2/\text{nDoF} < 8$,
- 78 • $(Z_{D_s} - Z_{B_s^0}) > 0$, where Z_M is the z-component of the position \vec{x} of the decay vertex
 79 for the B_s^0/D_s meson.

80 Additionally, we veto various physical backgrounds, which have either the same final
 81 state as our signal decay, or can contribute via a single misidentification of $K \rightarrow \pi$ or
 82 $K \rightarrow p$. In the following, the vetoes are ordered by the reconstructed D_s final state they
 83 apply to:

84 1. All:

- 85 (a) $B_s^0 \rightarrow D_s^+ D_s^-$: $|M(K\pi\pi) - m_{D_s}| > 20$ MeV/ c^2 .
- 86 (b) $B_s^0 \rightarrow D_s^- K^+ K^- \pi^+$: possible with single missID of $K^- \rightarrow \pi^-$, rejected by
 87 requiring π^- to fulfill $\text{DLL}_{K\pi} < 5$.

88 2. $D_s \rightarrow KK\pi$

- 89 (a) $B^0 \rightarrow D^+(\rightarrow K^+\pi^-\pi^+) K\pi\pi$: possible with single missID of $\pi^+ \rightarrow K^+$, vetoed
 90 by changing particle hypothesis and recompute $|M(K^+\pi^-\pi^+) - m_{D_p}| > 30$
 91 MeV/ c^2 , or the K^+ has to fulfill $\text{DLL}_{K\pi} > 10$.

- 92 (b) $\Lambda_b^0 \rightarrow \Lambda_c^+ (\rightarrow p K^- \pi^+) K \pi \pi$: possible with single missID of $p \rightarrow K^+$, vetoed by
 93 changing particle hypothesis and recompute $M(p K^- \pi^+) - m_{\Lambda_c^+} > 30 \text{ MeV}/c^2$,
 94 or the K^+ has to fulfill $(\text{DLL}_{K\pi} - \text{DLL}_{p\pi}) > 5$.
 95 (c) $D^0 \rightarrow KK$: D^0 combined with a random π can fake a $D_s \rightarrow KK\pi$ decay and
 96 be a background to our signal, vetoed by requiring $M(KK) < 1840 \text{ MeV}/c^2$.

97 3. $D_s \rightarrow \pi\pi\pi$

- 98 (a) $D^0 \rightarrow \pi\pi$: combined with a random π can fake a $D_s \rightarrow \pi\pi\pi$ decay and be a
 99 background to our signal, vetoed by requiring both possible combinations to
 100 have $M(\pi\pi) < 1700 \text{ MeV}/c^2$.

101 The most prominent final state used in this analysis is $B_s^0 \rightarrow D_s (\rightarrow KK\pi) K \pi \pi$, where
 102 the D_s decay can either proceed via the narrow ϕ resonance, the broader K^{*0} resonance, or
 103 non resonant. Depending on the decay process being resonant or not, we apply additional
 104 PID requirements on this final state:

- 105 • resonant case:

- 106 – $D_s^+ \rightarrow \phi \pi^+$, with $|M(K^+ K^-) - m_\phi| < 20 \text{ MeV}/c^2$: no additional requirements,
 107 since ϕ is narrow and almost pure $K^+ K^-$.
- 108 – $D_s^+ \rightarrow \bar{K}^{*0} K^+$, with $|M(K^- \pi^+) - m_{K^{*0}}| < 75 \text{ MeV}/c^2$: $\text{DLL}_{K\pi} > 0$ for kaons,
 109 since this resonance is more than ten times broader than ϕ .

- 110 • non resonant case: $\text{DLL}_{K\pi} > 5$ for kaons, since the non resonant category has
 111 significant charmless contributions.

112 For the $D_s \rightarrow \pi\pi\pi$ final state, we apply global PID requirements:

- 113 • $\text{DLL}_{K\pi} < 10$ for all pions.
 114 • $\text{DLL}_{p\pi} < 10$ for all pions.

115 3.2 Multivariate stage

116 We use TMVA [5] to train a multivariate discriminator, which is used to further improve
 117 the signal to background ratio. The 17 variables used for the training are:

- 118 • $\max(\text{ghostProb})$ over all tracks
 119 • $\text{cone}(p_T)$ asymmetry of every track, which is defined to be the difference between the
 120 p_T of the π/K and the sum of all other p_T in a cone of radius $r = \sqrt{(\Delta\Phi)^2 + (\Delta\eta)^2}$
 121 $< 1 \text{ rad}$ around the signal π/K track.
 122 • $\min(\text{IP}\chi^2)$ over the X_s daughters
 123 • $\max(\text{DOCA})$ over all pairs of X_s daughters
 124 • $\min(\text{IP}\chi^2)$ over the D_s daughters

- 125 • D_s and B_s^0 DIRA
 126 • D_s FD significance
 127 • $\max(\cos(D_s h_i))$, where $\cos(D_s h_i)$ is the cosine of the angle between the D_s and
 128 another track i in the plane transverse to the beam
 129 • B_s^0 IP χ^2 , FD χ^2 and Vertex χ^2

130 Various classifiers were investigated in order to select the best performing discriminator.
 131 Consequently, a boosted decision tree with gradient boost (BDTG) is chosen as nominal
 132 classifier. We use truth-matched MC as signal input. Simulated signal candidates are
 133 required to pass the same trigger, stripping and preselection requirements, that were
 134 used to select the data samples. For the background we use events from the high mass
 135 sideband ($m_{B_s^0 \text{candidate}} > 5600 \text{ MeV}/c^2$) of our data samples. As shown in Fig. 3.1,
 136 this mass region is sufficiently far away from signal structures and is expected to be
 137 dominantly composed of combinatorial background. For completeness, the mass distribu-
 138 tion of preselected $D_s \rightarrow hh$ candidates (where $h = \pi$ or $h = K$) is also shown in Fig. 3.1.

139

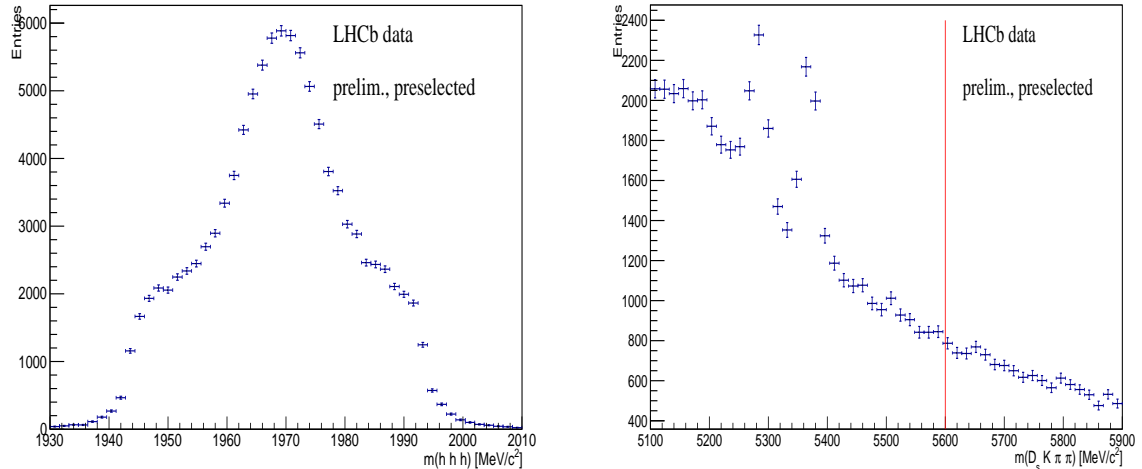


Figure 3.1: Invariant mass distribution of preselected (left) $D_s \rightarrow hh$ and (right) $B_s^0 \rightarrow D_s K \pi \pi$ candidates. For the $B_s^0 \rightarrow D_s K \pi \pi$ candidates, the region right from the red coloured line with $m_{B_s^0 \text{candidate}} > 5600 \text{ MeV}/c^2$ is used as background input for the boosted decision tree.

140 The distributions of the input variables for signal and background are shown in Fig.
 141 3.2.

142 The relative importance of the input variables for the BDTG training is summarized
 143 in Table 3.1.

144 The BDTG output distribution for test and training samples is shown in Fig 3.3. No
 145 sign of overtraining is observed.

146 We determine the optimal cut value by maximizing the figure of merit $S/\sqrt{S + B}$
 147 where S is the signal yield and B the background yield in the signal region, defined to be
 148 within $\pm 50 \text{ MeV}/c^2$ of the nominal B_s^0 mass. To avoid a bias in the determination of the
 149 branching fraction, we determine S and B using our normalization channel. All trigger,

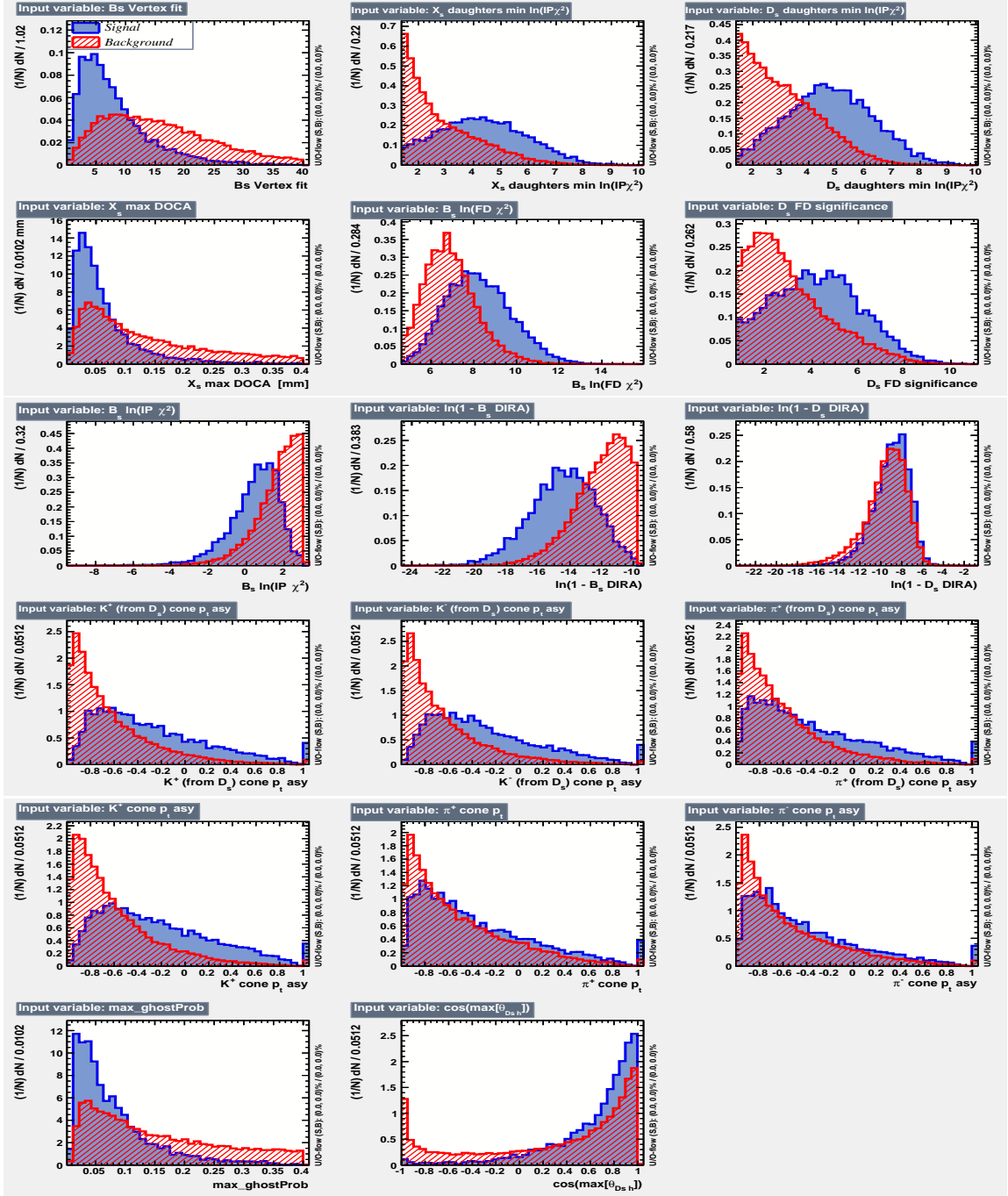


Figure 3.2: Distributions of the input variables used in the BDTG training. The background is shown as red hatched, while the signal is depicted solid blue.

stripping and additional selection criteria described in this and the previous chapter are applied to the $B_s^0 \rightarrow D_s \pi\pi\pi$ data samples. After that, we perform a simplified version of the fit to the invariant mass distribution of $B_s^0 \rightarrow D_s \pi\pi\pi$ candidates described in Sec. ???. Here, a Gaussian function to model the signal and an exponential function to model combinatorial background is used. From this fit we estimate the number of signal events in our normalization channel. Multiplying that number with the PDG branching fraction of $\frac{\mathcal{B}(B_s^0 \rightarrow D_s K\pi\pi)}{\mathcal{B}(B_s^0 \rightarrow D_s \pi\pi\pi)}$ and the ratio of efficiencies discussed in Sec. ?? allows us to estimate the

Variable	relative importance [%]
pi_minus_ptasy_1.00	7.32
log_Ds_FDCHI2_ORIVX	7.23
K_plus_ptasy_1.00	7.17
log_Ds_DIRA	6.96
Bs_ENDVERTEX_CHI2	6.82
max_ghostProb	6.76
pi_plus_ptasy_1.00	6.57
log_DsDaughters_min_IPCHI2	6.21
log_Bs_DIRA	6.15
K_plus_fromDs_ptasy_1.00	6.10
log_XsDaughters_min_IPCHI2	5.87
K_minus_fromDs_ptasy_1.00	5.62
cos(Ds h)	5.58
log_Bs_IPCHI2_OWNPV	5.08
log_Bs_FDCHI2_OWNPV	4.04
Xs_max_DOCA	3.98
pi_minus_fromDs_ptasy_1.00	2.59

Table 3.1: Summary of the relative importance of each variable in the training of the BDTG.

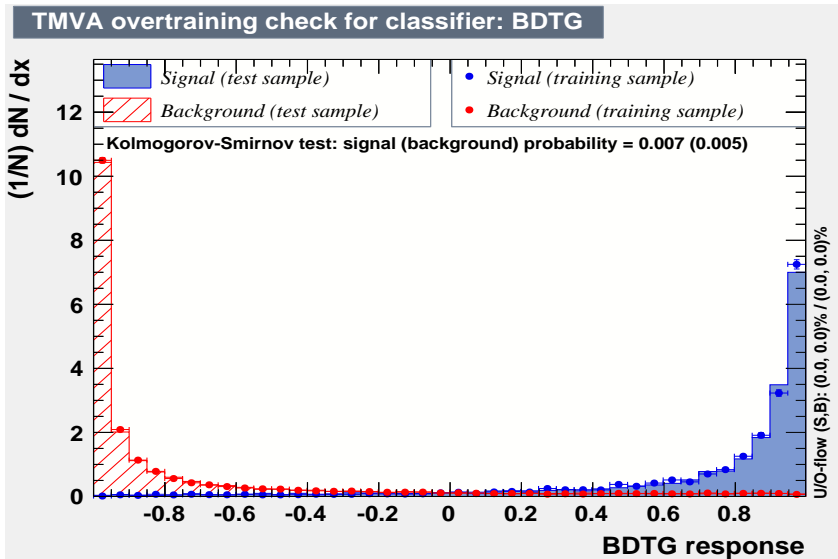


Figure 3.3: BDTG output classifier distribution for (blue) signal and (red) background. The response of an independent test sample (dots) is overlaid.

expected number of $B_s^0 \rightarrow D_s K\pi\pi$ signal decays. The number of background events can then be computed as

$$N_{bkg} = N_{all} - N_{sig}|_{m_{B_s^0 \pm 50 \text{ MeV}/c^2}}. \quad (3.1)$$

The efficiency curves as a function of the cut value are shown in Fig. 3.4. The optimal cut value is found to be BDTG > 0.7012. At this working point the signal efficiency is estimated to be 72.47 %, while the background rejection in the signal region is 97.38 %.

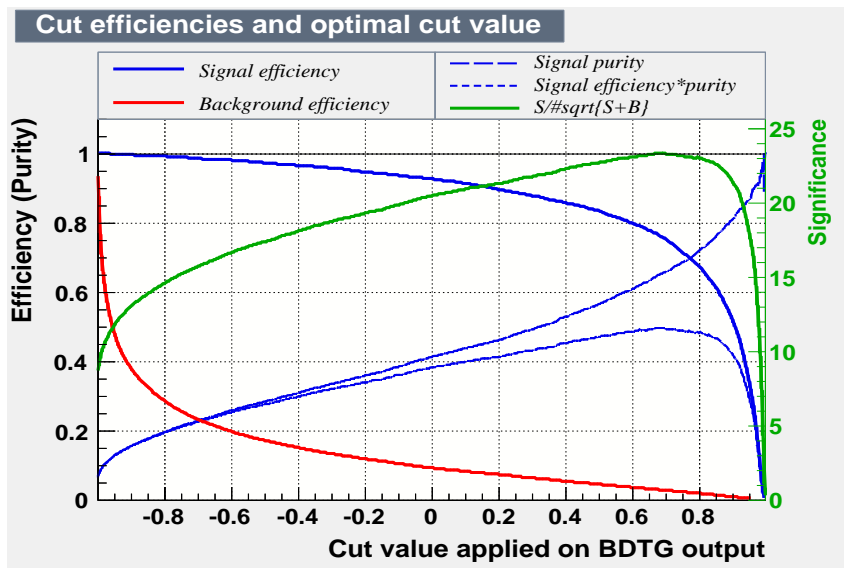


Figure 3.4: Efficiency and purity curves for (blue) signal, (red) background and the (green) FoM curve, as a function of the chosen cut value.

162 **4 Fits to invariant mass distributions of signal and**
 163 **normalization channel**

164 In order to properly model the invariant mass distribution of $B_s^0 \rightarrow D_s K \pi \pi$ and $B_s^0 \rightarrow$
 165 $D_s \pi \pi \pi$ candidates, the expected signal shape, as well as the expected shape for the
 166 combinatorial and physical background has to be known. This model can then be used to
 167 fit the distributions and obtain signal sWeights [?], which are employed to suppress the
 168 residual background that is still left in the sample, for the time-dependent amplitude fit.

169 **4.1 Signal models for $m(D_s \pi \pi \pi)$ and $m(D_s K \pi \pi)$**

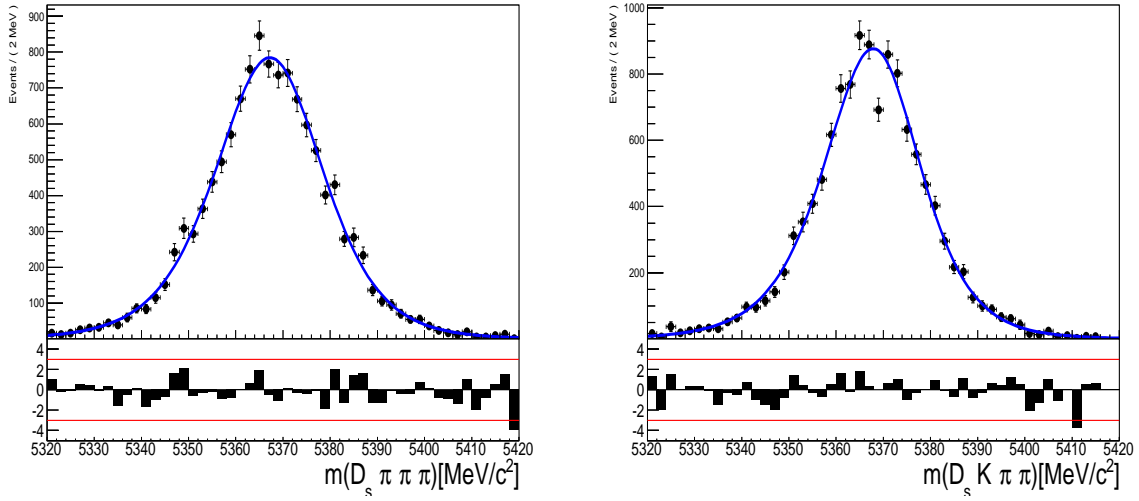


Figure 4.1: Invariant mass distributions of simulated (left) $B_s^0 \rightarrow D_s \pi \pi \pi$ and (right) $B_s^0 \rightarrow D_s K \pi \pi$ events. A fit of a RooJohnsonSU function to each distribution is overlaid.

170 The mass distribution of $B_s^0 \rightarrow D_s K \pi \pi$ signals is modeled using a Johnson SU
 171 function [?], which is a gaussian function with a Landau-like tail on one side,

$$J(m_{B_s^0}; \mu, \sigma, \gamma, \delta) = \frac{\delta}{\sigma 2\pi \sqrt{1 + (\frac{m_{B_s^0} - \mu}{\sigma})^2}} \exp\left(-\frac{1}{2}[\gamma + \delta \operatorname{Argsh}(\frac{m_{B_s^0} - \mu}{\sigma})]^2\right). \quad (4.1)$$

172 The sign of γ in Eq. 4.1 determines whether the tail is located at lower ($\gamma > 0$)
 173 or higher ($\gamma < 0$) invariant mass values than the mean μ of the gaussian function and
 174 δ describes the (a)symmetry of the fitted distribution. Higher values of δ result in a
 175 more symmetric, gaussian-like function. Another Johnson SU function function is used
 176 to account for the contribution of the $B^0 \rightarrow D_s K \pi \pi$ decay, which is also present in
 177 the $m(D_s K \pi \pi)$ spectrum. The width, as well as the tail parameters are fixed to values
 178 obtained by a fit to the invariant mass distribution of simulated events shown in Fig 4.1.
 179 A linear scaling factor for the mean μ and width σ is floated in the fit to account for
 180 possible differences between the simulation and real data.

181 The same approach is used to describe the invariant mass distribution of $B_s^0 \rightarrow D_s \pi \pi \pi$

182 candidates. A Johnson SU function is used to model the signal, the parameters are
183 determined by a fit to the invariant mass of simulated $B_s^0 \rightarrow D_s\pi\pi\pi$ decays, shown in
184 Fig 4.1. A scale factor for the width and the mean is floated to account for differences
185 between data and MC.

186 4.2 Background models for $m(D_s\pi\pi\pi)$

187 Different background sources arise in the invariant mass spectrum of candidates in the
188 normalization mode.

189 The following backgrounds have to be accounted for:

- 190 • Combinatorial background: This contribution arises from either a real D_s , which is
191 paired with random tracks to form the B_s^0 candidates, or via real X_d 's, which are
192 combined with three tracks that fake a D_s candidate to form a fake B_s^0 .
- 193 • Partially reconstructed $B^0/B_s^0 \rightarrow D_s^*\pi\pi\pi$ decays, with $D_s^* \rightarrow D_s\gamma$ or $D_s^* \rightarrow D_s\pi^0$,
194 where the γ/π^0 is not reconstructed in the decay chain.

195 In both cases of combinatorial background, the distribution in the invariant mass of
196 B_s^0 candidates is expected to be smooth and decrease with higher masses. Therefore, one
197 exponential function is used to model these contributions.

198 The shape of the $B_s^0 \rightarrow D_s^*\pi\pi\pi$ contribution is expected to be peaking in the $m(D_s\pi\pi\pi)$
199 spectrum, with large tails due to the missing momentum, which is carried away by the π^0
200 or γ . The pion or photon from $D_s^* \rightarrow D_s(\gamma/\pi^0)$ is excluded from the reconstruction. We
201 model the shape of this contribution using the sum of three bifurcated Gaussian functions.
202 The shape parameters, as well as the yield of this contribution, are directly determined
203 on data from a fit to the $m(D_s\pi\pi\pi)$ invariant mass distribution.

204 4.3 Background models for $m(D_sK\pi\pi)$

205 For the signal channel, the following background sources have to be considered:

- 206 • Combinatorial background: same contributions as discussed in Sec. 4.2.
- 207 • Partially reconstructed $B_s^0 \rightarrow D_s^*K\pi\pi$ decays, with $D_s^* \rightarrow D_s\gamma$ or $D_s^* \rightarrow D_s\pi^0$,
208 where the γ/π^0 is not reconstructed in the decay chain.
- 209 • Partially reconstructed $B^0 \rightarrow D_s^*K\pi\pi$ decays, with $D_s^* \rightarrow D_s\gamma$ or $D_s^* \rightarrow D_s\pi^0$,
210 where the γ/π^0 is not reconstructed in the decay chain.
- 211 • Misidentified $B_s^0 \rightarrow D_s\pi\pi\pi$ decays, where one of the pions is wrongly identified as a
212 kaon $\pi \rightarrow K$.
- 213 • Misidentified, partially reconstructed $B_s^0 \rightarrow D_s^*\pi\pi\pi$ decays, where one of the pions
214 is wrongly identified as a kaon $\pi \rightarrow K$ and the γ/π^0 from $D_s^* \rightarrow D_s\gamma/\pi^0$ is not
215 reconstructed.

216 The combinatorial background is expected to be non-peaking in the spectrum of the
217 invariant mass of $B_s^0 \rightarrow D_sK\pi\pi$ candidates. An exponential function is used to model
218 this contribution.

219 The shape of the partially reconstructed background without misID is taken from our
 220 normalization channel, where it can be directly fitted by the sum of three bifurcated
 221 Gaussian functions as described above. In the signal mass fit, all shape parameters for
 222 the $B_s^0 \rightarrow D_s^* K\pi\pi$ background are fixed to the input values from our normalization fit.

223 For the contribution of the $B^0 \rightarrow D_s^* K\pi\pi$ background, the same shape is used but
 224 the means μ_i of the bifurcated gaussians are shifted down by $m_{B_s^0} - m_{B^0}$ [?]. The yields
 225 of both contributions are directly determined in the nominal fit.

226 To determine the shape of misidentified $B_s^0 \rightarrow D_s \pi\pi\pi$ candidates in the $m(D_s K\pi\pi)$
 227 spectrum, we take a truth-matched signal MC sample of our normalization channel. We
 228 then use the PIDCalib package to determine the $\pi \rightarrow K$ fake rate. For every candidate
 229 in our MC sample, a (momentum) p and (pseudorapidity) η -dependent event weight is
 230 computed and assigned. We flip the particle hypothesis from pion to kaon for the π with
 231 the biggest miss-ID weight for each event and recompute the invariant B_s^0 mass. This
 232 distribution is then modeled using two Crystal Ball functions. The distribution and the
 233 fit are shown in Fig. 4.2(left).

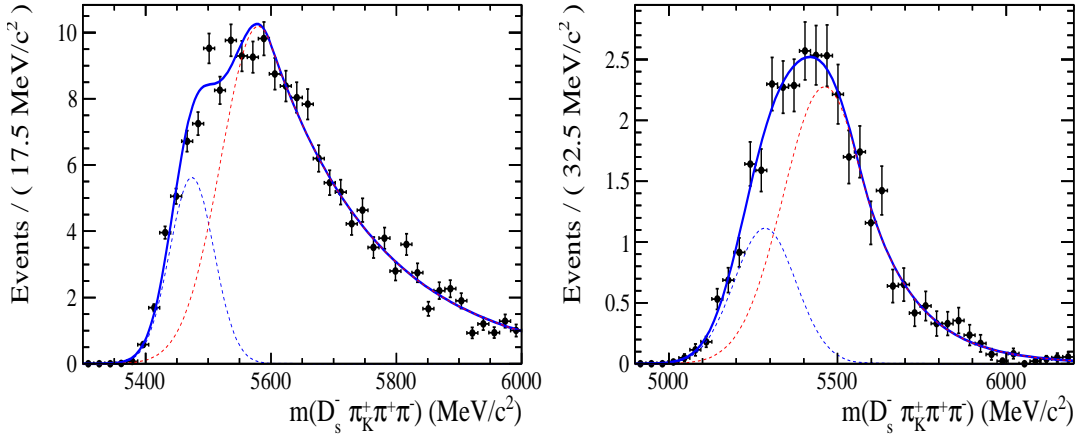


Figure 4.2: Invariant mass distribution of (left) simulated $B_s^0 \rightarrow D_s \pi\pi\pi$ events, where one of the π 's is reconstructed as a K and the misID probability for each event is taken into account. The corresponding distribution for simulated $B_s^0 \rightarrow D_s^* \pi\pi\pi$ events, where the γ/π^0 from the D_s^* is excluded from reconstruction, is shown on the right. The solid, black curve on each plot corresponds to the fit consisting of two Crystal Ball functions.

234 The expected yield of misidentified $B_s^0 \rightarrow D_s \pi\pi\pi$ candidates in the $m(D_s K\pi\pi)$ spec-
 235 trum is computed by multiplying the fake probability of $\propto 3.2\%$, which is derived from
 236 PIDCalib, by the yield of $B_s^0 \rightarrow D_s \pi\pi\pi$ signal candidates, determined in the nominal
 237 mass fit of our normalization channel.

238 In the same way as mentioned above, we can determine the rate of misidentified, partially
 239 reconstructed $B_s^0 \rightarrow D_s^* \pi\pi\pi$ decays in our sample of $B_s^0 \rightarrow D_s K\pi\pi$ decays using PIDCalib
 240 and a MC sample of $B_s^0 \rightarrow D_s^* \pi\pi\pi$ events. The invariant mass distribution we obtain
 241 when we exclude the γ/π^0 , flip the the particle hypothesis $\pi \rightarrow K$ and apply the event
 242 weights given by the fake rate, is shown in Fig. 4.2 (right). The fit of two Crystal Ball
 243 functions to this distribution is overlaid. The yield of this contribution is determined
 244 from the yield of $B_s^0 \rightarrow D_s^* \pi\pi\pi$ candidates in the nominal mass fit of our normalization
 245 channel, multiplied by the misID probability of $\propto 3.6\%$.

246 4.4 Fit to $B_s^0 \rightarrow D_s\pi\pi\pi$ candidates

247 An unbinned maximum likelihood fit is performed simultaneously to the invariant mass
 248 distribution of $B_s^0 \rightarrow D_s\pi\pi\pi$ candidates. As discussed in Sec. 4.1, the fit is given
 249 as a Johnson SU signal model for the B_s^0 and B^0 signal, the sum of three bifurcated
 250 Gaussian functions to model the partially reconstructed $B_s^0 \rightarrow D_s^*\pi\pi\pi$ background and
 251 an Exponential function to account for combinatorial background. The invariant mass
 252 distribution and the fit is shown in Fig. 4.3. All simultaneously performed fits to the
 253 $m(D_s\pi\pi\pi)$ distribution, ordered by the respective D_s final state, can be found in the
 254 Appendix ???. The obtained yields are summarized in Table 4.1.

255 4.5 Fit to $B_s^0 \rightarrow D_sK\pi\pi$ candidates

256 The shape of the invariant mass distribution of $B_s^0 \rightarrow D_sK\pi\pi$ candidates is described by
 257 Johnson SU functions for the B^0 and B_s^0 signal, two sums of three bifurcated Gaussians
 258 for the $B_s^0/B^0 \rightarrow D_s^*K\pi\pi$ partially reconstructed background contributions and two
 259 sums of double Crystal Ball functions for the single misID $B_s^0 \rightarrow D_s\pi\pi\pi$ and the partially
 260 reconstructed, misidentified $B_s^0 \rightarrow D_s^*\pi\pi\pi$ decays. A simultaneous unbinned maximum
 261 likelihood fit is performed and the result is shown in Fig. 4.3. All simultaneously performed
 262 fits to the $m(D_sK\pi\pi)$ distribution, ordered by the respective D_s final state, can be found
 263 in the Appendix ???. The obtained yields are summarized in Table 4.1.

264 4.6 Extraction of signal weights

265 The sPlot technique [?] is used to extract signal weights from the fits to the invariant
 266 mass distributions of our signal and normalization channel. This statistical tool assigns
 267 a weight to every event, according to its position in the respective mass distribution,
 268 given the fitted signal and background models. The weights can then be used to suppress
 269 the background components in every other observable distribution of interest. Figure 4.4
 270 shows the distribution of weights across the invariant mass spectra of $B_s^0 \rightarrow D_s\pi\pi\pi$ and
 271 $B_s^0 \rightarrow D_sK\pi\pi$ candidates.

fit component	yield 2011	yield 2012	yield 2015	yield 2016
$m(D_sK\pi\pi)$				
$B_s^0 \rightarrow D_sK\pi\pi$	392 ± 25	860 ± 38	309 ± 21	1984 ± 55
$B^0 \rightarrow D_sK\pi\pi$	276 ± 26	692 ± 41	261 ± 23	1385 ± 58
$B^0/B_s^0 \rightarrow D_s^*K\pi\pi$	7 ± 25	171 ± 75	114 ± 25	893 ± 84
$B_s^0 \rightarrow D_s^{(*)}\pi\pi\pi$	63 ± 0	158 ± 0	53 ± 0	314 ± 0
combinatorial	1482 ± 53	2884 ± 100	605 ± 43	4261 ± 133
$m(D_s\pi\pi\pi)$				
$B_s^0 \rightarrow D_s\pi\pi\pi$	9183 ± 105	22083 ± 166	7574 ± 95	43773 ± 245
$B^0 \rightarrow D_s\pi\pi\pi$	289 ± 58	716 ± 95	229 ± 54	968 ± 147
$B_s^0 \rightarrow D_s^*\pi\pi\pi$	3640 ± 130	9086 ± 232	3047 ± 110	17827 ± 421
combinatorial	4991 ± 154	11127 ± 271	3728 ± 126	24589 ± 500

Table 4.1: Summary of yields obtained from the fits to Run1 and Run2 data.

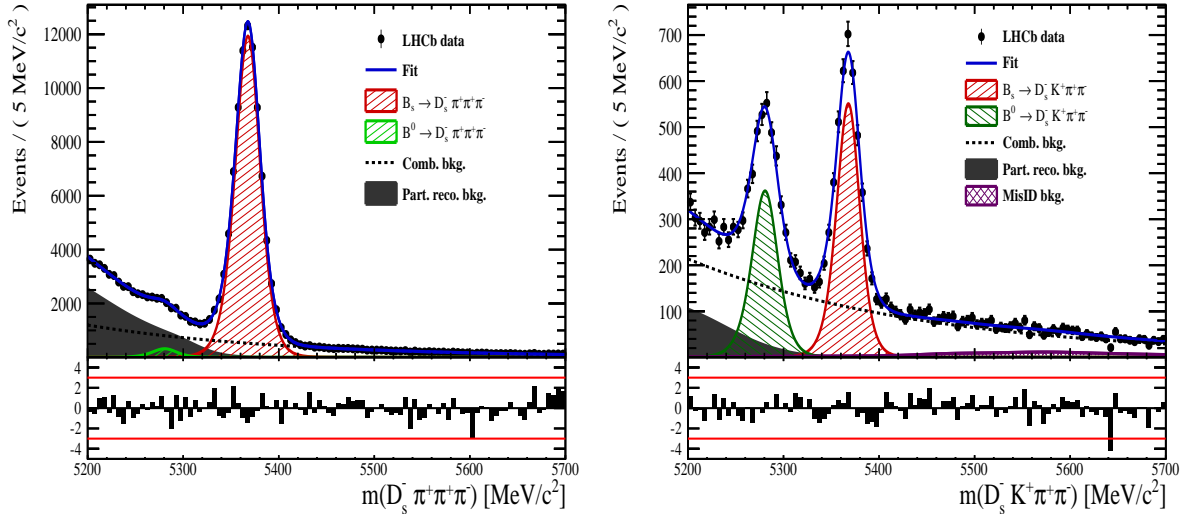


Figure 4.3: Invariant mass distribution of (left) $B_s^0 \rightarrow D_s \pi\pi\pi$ and (right) $B_s^0 \rightarrow D_s K\pi\pi$ candidates for Run1 and Run2 data. The respective fit described in the text is overlaid.

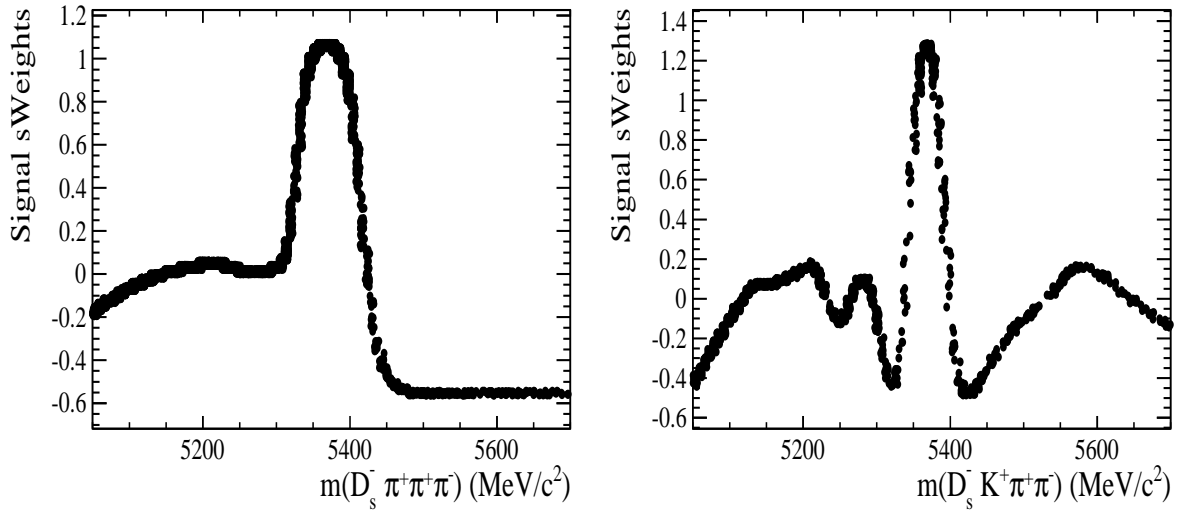


Figure 4.4: Distribution of sWeights across the invariant mass of (left) $B_s^0 \rightarrow D_s \pi\pi\pi$ and (right) $B_s^0 \rightarrow D_s K\pi\pi$ candidates for Run1 and Run2 data.

272 5 Flavour Tagging

273 To successfully perform a time- and amplitude-dependent measurement of γ , the identifi-
 274 cation of the initial state flavour of the B_s^0 meson is crucial. In the presented analysis,
 275 a number of flavour tagging algorithms are used that either determine the flavour of
 276 the non-signal b-hadron produced in the event (opposite site, OS), or they use particles
 277 produced in the fragmentation of the signal candidate B_s^0/\bar{B}_s^0 (same side, SS).
 278 For the same side, the algorithm searching for the charge of an additional kaon that accom-
 279 panies the fragmentation of the signal candidate is used (SS-nnetKaon). For the opposite
 280 site, four different taggers are chosen: The Two algorithms that use the charge of an
 281 electron or a muon from semileptonic B decays (OS- e,μ), the tagger that uses the charge
 282 of a kaon from a $b \rightarrow c \rightarrow s$ decay chain (OS-nnetKaon) and the algorithm that determines
 283 the B_s^0/\bar{B}_s^0 candidate flavour from the charge of a secondary vertex, reconstructed from
 284 the OS b decay product (OS-VtxCharge). All four taggers are then combined into a signal
 285 OS tagger.
 286 Every single tagging algorithm is prone to misidentify the signal candidate at a certain
 287 mistag rate $\omega = (\text{wrongtags})/(\text{alltags})$. This might be caused by particle misidentifica-
 288 tion, flavour oscillation of the neutral opposite site B-meson or by tracks that are wrongly
 289 picked up from the underlying event. For every signal B_s^0/\bar{B}_s^0 candidate, each tagging
 290 algorithm predicts a mistag probability η , which is calculated using a combination of
 291 inputs such as the kinematics of the tagging particles. The inputs are then combined
 292 to a predicted mistag using neural networks. These are trained on simulated samples
 293 of $B_s^0 \rightarrow D_s^- \pi^+$ (SS algorithm) and $B^+ \rightarrow J/\psi K^+$ (OS algorithms) decays. For the
 294 presented analysis, the measurable CP-violating coefficients are damped by the tagging
 295 dilution D , that depends on the mistag rate:

$$D = 1 - 2\omega. \quad (5.1)$$

296 This means that the statistical precision, with which these coefficients can be measured,
 297 scales as the inverse square root of the effective tagging efficiency,

$$\epsilon_{eff} = \epsilon_{tag}(1 - 2\omega)^2, \quad (5.2)$$

298 where ϵ_{tag} is the fraction of events that have a tagging decision. The flavour
 299 tagging algorithms are optimised for highest ϵ_{eff} on data, using the $B_s^0 \rightarrow D_s^- \pi^+$ and
 300 $B^+ \rightarrow J/\psi K^+$ samples.

301 Utilizing flavour-specific final states, the predicted mistag η of each tagger has to be
 302 calibrated to match the observed mistag ω on the data sample. For the calibration, a
 303 linear model of the form

$$\omega(\eta) = p_0 + p_1 \cdot (\eta - \langle \eta \rangle), \quad (5.3)$$

304 where the values of p_0 and p_1 are determined using the $B_s^0 \rightarrow D_s \pi \pi \pi$ normalization
 305 mode and $\langle \eta \rangle$ is the average estimated mistag probability $\langle \eta \rangle = \sum_{i=1}^{N_{cand}} (\eta_i)/N_{cand}$.
 306 Following this model, a perfectly calibrated tagger would lead to $\omega(\eta) = \eta$ and one would
 307 expect $p_1 = 1$ and $p_0 = \langle \eta \rangle$. Due to the different interaction cross-sections of oppositely
 308 charged particles, the tagging calibration parameters depend on the initial state flavour of
 309 the B_s^0 . Therefore, the flavour asymmetry parameters Δp_0 , Δp_1 and $\Delta \epsilon_{tag}$ are introduced.
 310 For this analysis, the calibrated mistag is treated as per-event variable, giving a larger

weight to events that are less likely to have an incorrect tag. This adds one additional observable to the time- and amplitude-dependent fit.
 The tagging calibration is determined using a time-dependent fit to the full $B_s^0 \rightarrow D_s\pi\pi\pi$ sample, where the mixing frequency Δm_s is fixed to the nominal PDG value [8]. The calibration procedure for the OS tagging algorithms (Sec.5.1) and the SS kaon tagger (Sec.5.2) is applied on the full Run I and 2015 and 2016 Run II $B_s^0 \rightarrow D_s\pi\pi\pi$ data sample, which is selected following the steps described in Sec. 3. The similar selection ensures as close as possible agreement between the $B_s^0 \rightarrow D_s\pi\pi\pi$ and $B_s^0 \rightarrow D_sK\pi\pi$ samples in terms of the decay kinematics, which are crucial for the flavour tagging. Section 5.3 shows the compatibility of both samples. After applying the calibration, the response of the OS and SS taggers are combined, which is shown in Sec. 5.4.

5.1 OS tagging calibration

The responses of the OS electron, muon, neural net kaon and the secondary vertex charge taggers are combined for the mistag calibration. Figure ?? shows the distribution of the predicted OS mistag for signal candidates from $B_s^0 \rightarrow D_s\pi\pi\pi$. The extracted calibration parameters and tagging asymmetries are summarized in Table 5.1 and the measured tagging power for the OS combination is $\epsilon_{eff,OS} = 4.81\%$.

p_0	p_1	$<\eta>$	ϵ_{tag}	Δp_o	Δp_1	$\epsilon_{eff} [\%]$
0.025 ± 0.005	0.944 ± 0.048	0.347	0.517 ± 0.002	0.028 ± 0.005	0.037 ± 0.045	$4.81 \pm 0.04 \text{ (stat)} \pm 0.37 \text{ (cal)}$

Table 5.1: Calibration parameters and tagging asymmetries of the OS tagger extracted from $B_s^0 \rightarrow D_s\pi\pi\pi$ decays.

5.2 SS tagging calibration

The SS neural net kaon tagger can be calibrated using the flavour-specific $B_s^0 \rightarrow D_s\pi\pi\pi$ decay. Its development, performance and calibration is described in detail in [?]. Figure ?? shows the distribution of the predicted mistag of the neural net kaon tagger. The extracted calibration parameters and tagging asymmetries are summarized in Table 5.2 and the measured tagging power for this algorithm is $\epsilon_{eff,SS} = 3.22\%$.

p_0	p_1	$<\eta>$	ϵ_{tag}	Δp_o	Δp_1	$\epsilon_{eff} [\%]$
0.008 ± 0.004	1.086 ± 0.059	0.381	0.571 ± 0.002	-0.017 ± 0.004	0.135 ± 0.058	$3.22 \pm 0.03 \text{ (stat)} \pm 0.26 \text{ (cal)}$

Table 5.2: Calibration parameters and tagging asymmetries of the SS tagger extracted from $B_s^0 \rightarrow D_s\pi\pi\pi$ decays.

5.3 Tagging performance comparison between the signal and normalization channel

To justify the usage of the tagging calibration, obtained using the $B_s^0 \rightarrow D_s\pi\pi\pi$ sample, for our signal decay, the performance of the taggers in the two decay channels needs to be compatible. This is verified using both, simulated signal samples of both decays and

339 sweighted data, to compare the similarity of the mistag probabilities, tagging decisions
 340 and kinematic observables that are correlated with the tagging response, on simulation
 341 and data.

342 The distributions of the predicted mistag probability η for the OS combination and the
 343 SS kaon tagger are shown in Fig. ?? (simulation) and Fig. 5.1 (data).

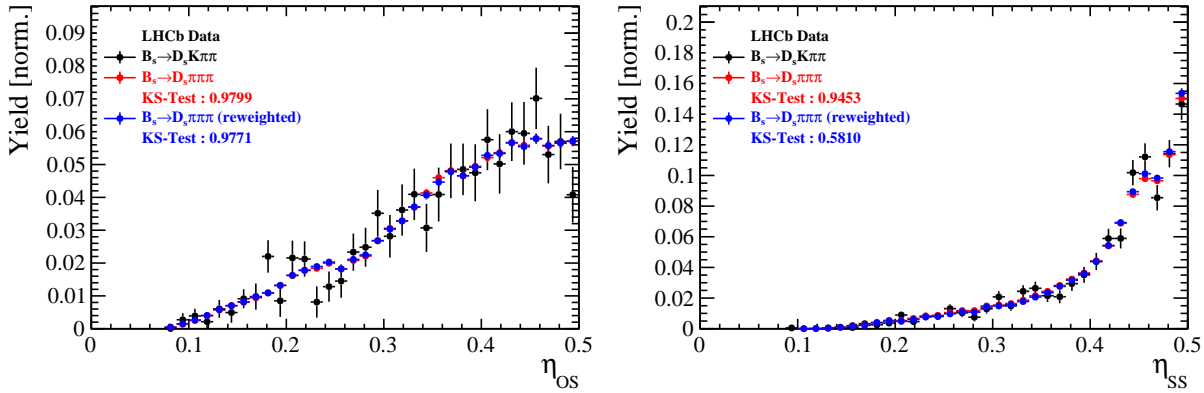


Figure 5.1: Distributions of the predicted mistag η for the OS combination (left) and the SS kaon tagger (right) for signal candidates in the $B_s^0 \rightarrow D_s K\pi\pi$ (black) and $B_s^0 \rightarrow D_s \pi\pi\pi$ (red) data samples.

344 Both, data and simulated samples, show good agreement between the signal and
 345 normalization channel. Compatibility is also seen in Fig. ??, which shows the comparison
 346 of the tagging decision distributions of the OS and SS tagger for sweighted data.

347 Fig. ?? shows the signal data distributions of the transverse B_s^0 momentum p_T , the
 348 pseudorapidity η of the signal candidate and the number of reconstructed tracks per event.
 349 Sufficient agreement is observed.

350 To justify the portability of the flavour tagging calibration obtained from $B_s^0 \rightarrow D_s \pi\pi\pi$
 351 to the $B_s^0 \rightarrow D_s K\pi\pi$ channel, besides the good agreement of the distributions shown
 352 above, the dependence of the measured mistag ω on the predicted mistag η has to be
 353 compatible in both channel. This dependence is shown in Fig. 5.2 for simulated signal
 354 events of both channels, where good agreement is observed.

355 5.4 Combination of OS and SS taggers

356 In the time- and amplitude-dependent fit to $B_s^0 \rightarrow D_s K\pi\pi$ data, the obtained tagging
 357 responses of the OS and SS tagger will be combined after the calibration described in the
 358 previous sections is applied. Events that acquire a mistag probability greater than 0.5 after
 359 the calibration will have their tagging decision flipped. For events where only one of the
 360 two taggers fired, the combination of the tagging decision is trivial. In those events where
 361 both taggers made a decision, we use the standard combination of taggers [?] provided
 362 by the flavour tagging group. In the nominal fit, the calibrated mistags ω are combined
 363 event by event for the OS and SS tagger, thus adding one variable to observable to the
 364 fit procedure. This ensures that the uncertainties of the OS and SS tagging calibration
 365 parameters are propagated properly to the combined tagging response for each event.
 366 The tagging performance for the combined tagger in the categories SS tagged only, OS
 367 tagged only and SS+OS tagged, are shown in Tab. ?? for the signal and normalization

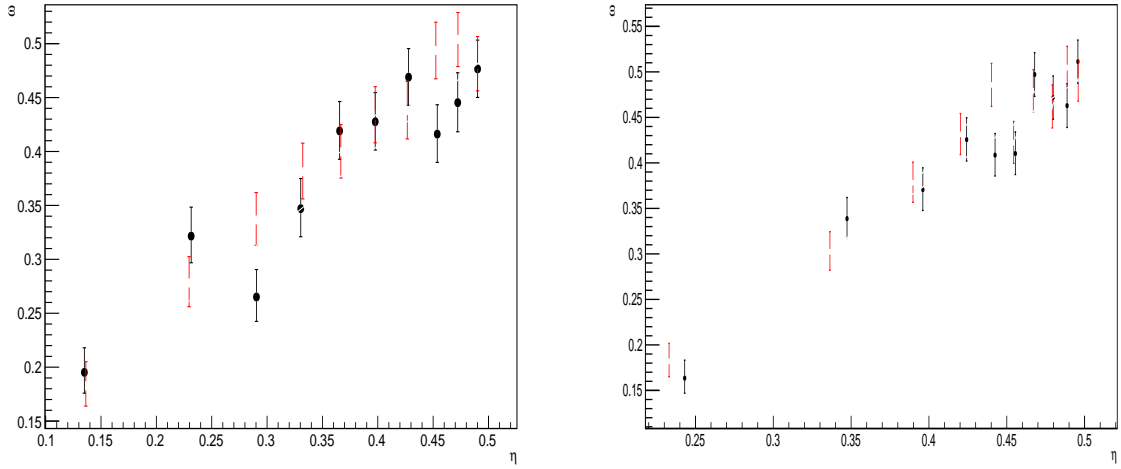


Figure 5.2: Dependence of the observed mistag ω on the predicted mistag η for the (left) OS combination and the (right) SS kaon tagger, found in the simulated $B_s^0 \rightarrow D_s K\pi\pi$ (black) and $B_s^0 \rightarrow D_s \pi\pi\pi$ (red) signal samples.

368 channel. The distribution of the observed mistag ω as a function of the combined mistag
 369 probability η for $B_s^0 \rightarrow D_s \pi\pi\pi$ decays is shown in Fig. 5.3.

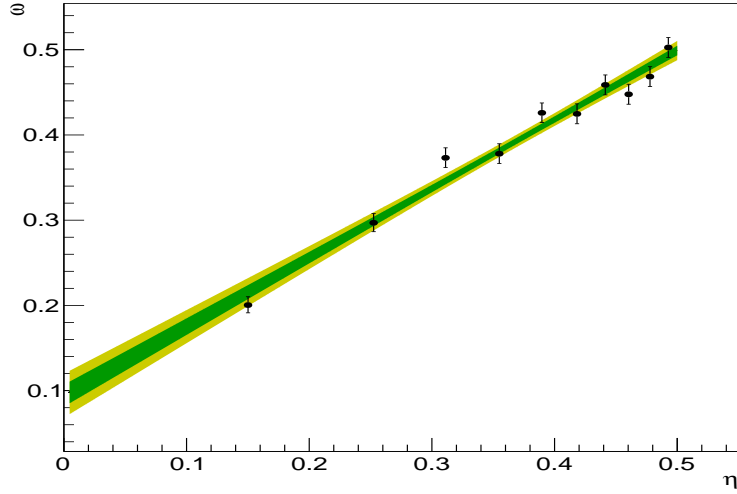


Figure 5.3: Distribution of the predicted combined mistag probability η versus the observed mistag ω for $B_s^0 \rightarrow D_s \pi\pi\pi$ signal candidates. The fit with a linear polynomial, used to determine p_0 and p_1 is overlaid.

$B_s^0 \rightarrow D_s\pi\pi\pi$		ϵ_{tag}	ϵ_{eff}
SS only		$(28.586 \pm 0.165)\%$	$(1.408 \pm 0.018(\text{stat}) \pm 0.082(\text{cal}))\%$
OS only		$(17.221 \pm 0.138)\%$	$(2.027 \pm 0.029(\text{stat}) \pm 0.100(\text{cal}))\%$
SS+OS		$(39.981 \pm 0.179)\%$	$(5.690 \pm 0.047(\text{stat}) \pm 0.196(\text{cal}))\%$
total			
$B_s^0 \rightarrow D_sK\pi\pi$		ϵ_{tag}	ϵ_{eff}
SS only		$(30.094 \pm 0.960)\%$	$(1.379 \pm 0.082(\text{stat}) \pm 0.085(\text{cal}))\%$
OS only		$(18.923 \pm 0.819)\%$	$(1.768 \pm 0.121(\text{stat}) \pm 0.099(\text{cal}))\%$
SS+OS		$(27.277 \pm 0.932)\%$	$(3.914 \pm 0.194(\text{stat}) \pm 0.220(\text{cal}))\%$
total			

Table 5.3: Flavour tagging performances for $B_s^0 \rightarrow D_s\pi\pi\pi$ and $B_s^0 \rightarrow D_sK\pi\pi$ events which are only OS tagged, only SS tagged or tagged by both.

370 6 Decay-time acceptance

371 The decay-time distribution of the B_s^0 mesons is sculpted due to the geometry of the LHCb
 372 detector and the applied selection cuts, which are described in Section 3. In particular,
 373 any requirement on the flight distance (FD), the impact parameter (IP) or the direction
 374 angle (DIRA) of the B_s^0 mesons, as well as the direct cut on the lifetime, will lead to a
 375 decay-time dependent efficiency $a(t)$. This efficiency will distort the theoretically expected,
 376 time-dependent decay rate

$$\frac{\Gamma(t)^{observed}}{dt} = \frac{\Gamma(t)^{theory}}{dt} \cdot a(t), \quad (6.1)$$

377 and has to be modelled correctly, in order to describe the observed decay rate. We
 378 use our control channel for this measurement, because for $B_s^0 \rightarrow D_s K\pi\pi$ decays the
 379 decay-time acceptance is correlated with the CP-observables which we aim to measure.
 380 Therefore, floating the CP-observables and the acceptance shape at the same time is
 381 not possible. Hence, a fit to the decay-time distribution of $B_s^0 \rightarrow D_s \pi\pi\pi$ candidates is
 382 performed and the obtained acceptance shape is corrected by the difference in shape found
 383 for the $B_s^0 \rightarrow D_s K\pi\pi$ and $B_s^0 \rightarrow D_s \pi\pi\pi$ MC.

384 A PDF of the form

$$\mathcal{P}(t', \vec{\lambda}) = \left[(e^{\Gamma_s t} \cdot \cosh(\frac{\Delta\Gamma_s t}{2}) \times \mathcal{R}(t - t')) \cdot \epsilon(t', \vec{\lambda}) \right], \quad (6.2)$$

385 is fit to the decay time distribution of $B_s^0 \rightarrow D_s \pi\pi\pi$ candidates in data. Since the
 386 fit is performed untagged, the PDF shown in Eq. 6.2 contains no terms proportional to
 387 Δm_s . The values for Γ_s and $\Delta\Gamma_s$ are fixed to the latest HFAG results [6]. The decay-
 388 time acceptance $\epsilon(t', \vec{\lambda})$ is modelled using the sum of cubic polynomials $v_i(t)$, so called
 389 Splines [7]. The polynomials are parametrised by so-called knots which determine their
 390 boundaries. Knots can be set across the fitted distribution to account for local changes in
 391 the acceptance shape. Using more knots is equivalent to using more base splines which
 392 are defined on a smaller sub-range. In total, $n + 2$ base splines $v_i(t)$ are needed to describe
 393 an acceptance shape which is parametrised using n knots.

394 For fits shown in the following, the knots have been placed at $t = [0.5, 1.0, 1.5, 2.0, 3.0, 9.5] ps$. To accommodate these 6 knot positions, 8 basic splines
 395 v_i , $i = [1, \dots, 8]$ are used. Since a rapid change of the decay time acceptance at low
 396 decay times due to the turn-on effect generated by the lifetime and other selection cuts is
 397 expected, more knots are placed in that regime. At higher decay times we expect linear
 398 behavior, with a possible small effect due to the VELO reconstruction. Therefore fewer
 399 knots are used. Furthermore, v_7 is fixed to 1 in order to normalize the overall acceptance
 400 function. To stabilise the last spline, v_8 is fixed by a linear extrapolation from the two
 401 previous splines:

$$v_N = v_{N-1} + \frac{v_{N-2} - v_{N-1}}{t_{N-2} - t_{N-1}} \cdot (t_N - t_{N-1}). \quad (6.3)$$

403 Here, $N = 8$ and t_{N-1} corresponds to the knot position associated with v_{N-1} .

404 6.1 Comparison of acceptance in subsamples

405 It is possible that the decay-time dependent efficiency deviates in different subsamples of
 406 our data. In particular, the acceptance could differentiate in subsamples with different
 407 final state kinematics, such as the run I & run II sample, the various D_s final states and
 408 the ways an event is triggered at the L0 stage. To investigate possible deviations, the
 409 full selected $B_s^0 \rightarrow D_s\pi\pi\pi$ sample is split into subsamples according to the categories
 410 mentioned above (run, D_s state, L0 trigger). For each subsample, the fit procedure
 411 described at the beginning of this chapter, using the pdf given by Eq. 6.2, is repeated
 412 and the obtained values for the spline coefficients v_i are compared. Figure 6.1 shows the
 413 comparison of the obtained spline coefficients for the different D_s final states.

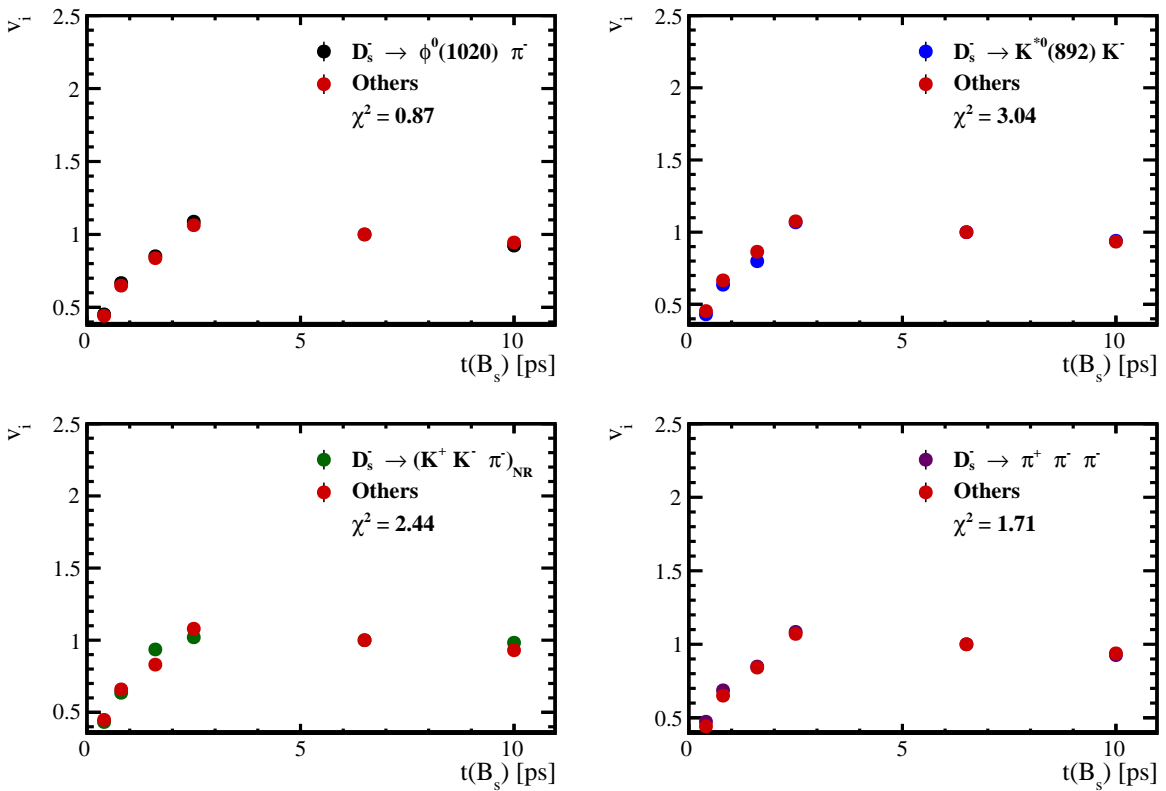


Figure 6.1: Comparison of the spline coefficients obtained from time-dependent fits to the $B_s^0 \rightarrow D_s\pi\pi\pi$ subsamples of different D_s final states. The comparison of one particular D_s state against all other states is shown.

414 Investigating the obtained spline coefficients from different D_s final states, good
 415 agreement is observed between all four channels and no need to distinguish between
 416 different final states in the time-dependent amplitude fit is found.

417 The comparison between spline coefficients for the different runs and L0 trigger categories
 418 is shown in Figure 6.2.

419 Significant deviations between spline coefficients obtained from the two different runs
 420 and L0 trigger categories can be observed. The deviations are most pronounced in the
 421 (0 – 5) ps region, where the majority of statistics is found. Therefore, the time-dependent
 422 efficiency has to be treated separately for the runs and L0 categories. This is achieved by

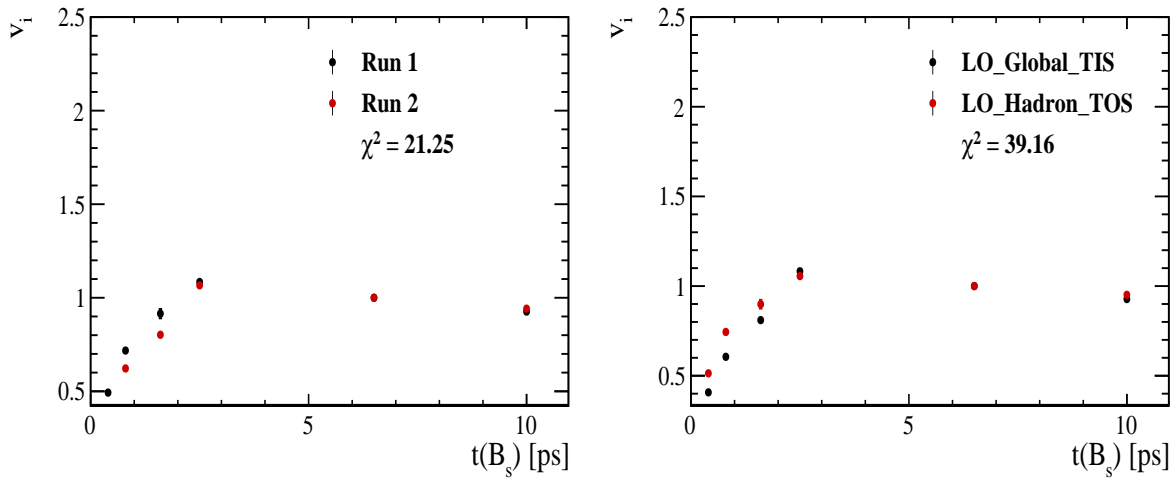


Figure 6.2: Comparison of the spline coefficients obtained from time-dependent fits to the $B_s^0 \rightarrow D_s \pi \pi \pi$ subsamples of (left) the different runs and (right) L0 trigger categories.

⁴²³ implementing a simultaneous fit, where the acceptance description is allowed to vary in
⁴²⁴ the subsamples.

6.2 Results

The nominal fit to $B_s^0 \rightarrow D_s\pi\pi\pi$ data using this configuration is shown in Figure 6.3. Note that the normalization of the splines in the following figures is not in scale. The fit parameters obtained from the described fits to data and simulation are summarised in Table 6.5.

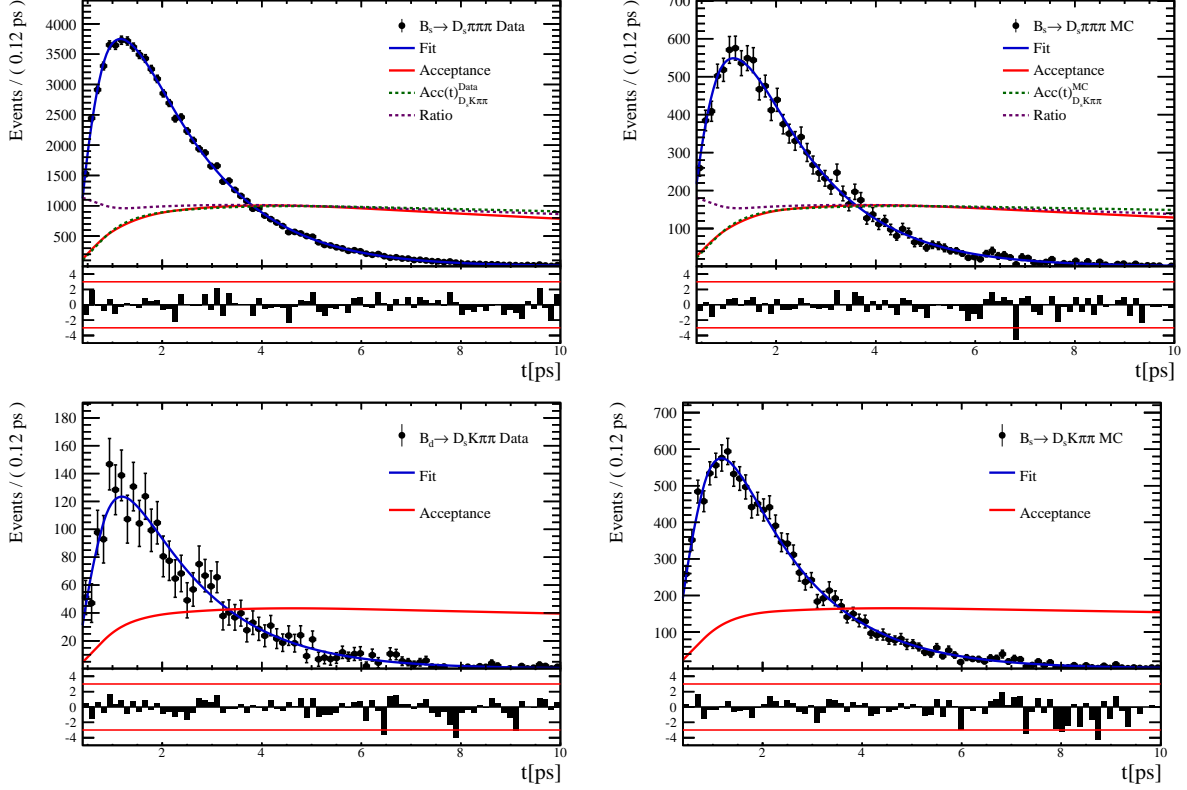


Figure 6.3: The red line shows the spline function describing the acceptance and the blue line depicts the total fit function.

Table 6.1: Summary of the obtained parameters from the acceptance fit

Knot position	Coefficient	$B_s^0 \rightarrow D_s K\pi\pi$ data	$B_s^0 \rightarrow D_s K\pi\pi$ MC	Ratio
0.4	v_0	0.446 ± 0.034	0.479 ± 0.022	1.020 ± 0.078
0.8	v_1	0.673 ± 0.051	0.702 ± 0.034	0.943 ± 0.069
1.6	v_2	0.874 ± 0.076	0.915 ± 0.054	0.984 ± 0.084
2.5	v_3	1.028 ± 0.043	1.021 ± 0.038	1.042 ± 0.043
6.5	v_4	1.000 ± 0.000	1.000 ± 0.000	1.000 ± 0.000
10.0	v_5	0.975 ± 0.000	0.982 ± 0.000	0.963 ± 0.000

Table 6.2: Summary of the obtained parameters from the acceptance fit

Knot position	Coefficient	$B_s^0 \rightarrow D_s K\pi\pi$ data	$B_s^0 \rightarrow D_s K\pi\pi$ MC	Ratio
0.4	v_0	0.425 ± 0.039	0.456 ± 0.025	1.054 ± 0.091
0.8	v_1	0.626 ± 0.058	0.673 ± 0.039	1.028 ± 0.095
1.6	v_2	0.936 ± 0.105	0.887 ± 0.067	0.955 ± 0.102
2.5	v_3	1.081 ± 0.066	1.050 ± 0.049	1.019 ± 0.069
6.5	v_4	1.000 ± 0.000	1.000 ± 0.000	1.000 ± 0.000
10.0	v_5	0.929 ± 0.000	0.956 ± 0.000	0.983 ± 0.000

Table 6.3: Summary of the obtained parameters from the acceptance fit

Knot position	Coefficient	$B_s^0 \rightarrow D_s K\pi\pi$ data	$B_s^0 \rightarrow D_s K\pi\pi$ MC	Ratio
0.4	v_0	0.615 ± 0.080	0.525 ± 0.039	0.935 ± 0.106
0.8	v_1	0.922 ± 0.124	0.751 ± 0.060	0.842 ± 0.110
1.6	v_2	0.940 ± 0.123	0.959 ± 0.083	1.025 ± 0.126
2.5	v_3	0.940 ± 0.077	0.949 ± 0.062	1.111 ± 0.059
6.5	v_4	1.000 ± 0.000	1.000 ± 0.000	1.000 ± 0.000
10.0	v_5	1.053 ± 0.000	1.045 ± 0.000	0.903 ± 0.000

Table 6.4: Summary of the obtained parameters from the acceptance fit

Knot position	Coefficient	$B_s^0 \rightarrow D_s K\pi\pi$ data	$B_s^0 \rightarrow D_s K\pi\pi$ MC	Ratio
0.4	v_0	0.385 ± 0.019	0.478 ± 0.018	1.014 ± 0.056
0.8	v_1	0.584 ± 0.028	0.695 ± 0.029	0.975 ± 0.055
1.6	v_2	0.802 ± 0.067	0.919 ± 0.052	0.967 ± 0.078
2.5	v_3	1.032 ± 0.048	1.021 ± 0.038	1.045 ± 0.047
6.5	v_4	1.000 ± 0.000	1.000 ± 0.000	1.000 ± 0.000
10.0	v_5	0.972 ± 0.000	0.982 ± 0.000	0.960 ± 0.000

Table 6.5: Summary of the obtained parameters from the acceptance fit

Knot position	Coefficient	$B_s^0 \rightarrow D_s K\pi\pi$ data	$B_s^0 \rightarrow D_s K\pi\pi$ MC	Ratio
0.4	v_0	0.481 ± 0.032	0.479 ± 0.020	1.015 ± 0.061
0.8	v_1	0.711 ± 0.050	0.698 ± 0.031	0.962 ± 0.067
1.6	v_2	0.905 ± 0.079	0.918 ± 0.052	0.972 ± 0.079
2.5	v_3	1.002 ± 0.061	1.020 ± 0.041	1.045 ± 0.055
6.5	v_4	1.000 ± 0.000	1.000 ± 0.000	1.000 ± 0.000
10.0	v_5	0.998 ± 0.000	0.982 ± 0.000	0.961 ± 0.000

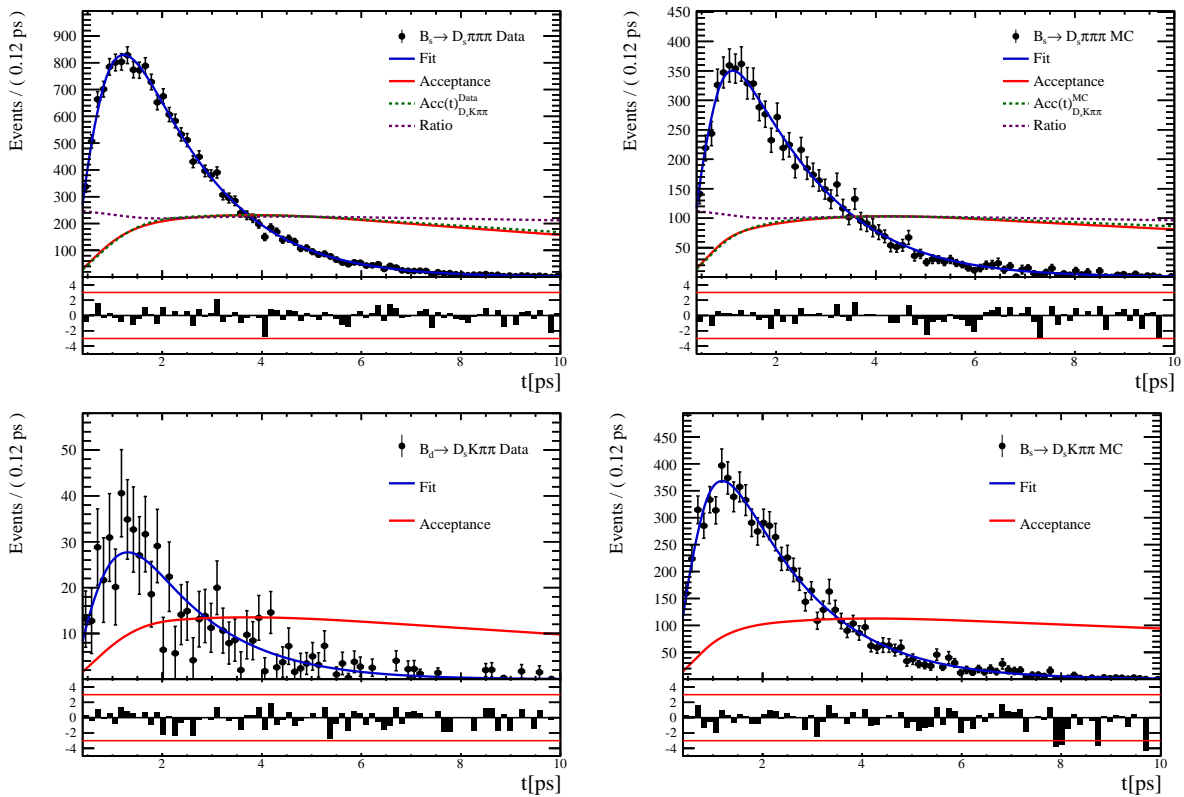


Figure 6.4

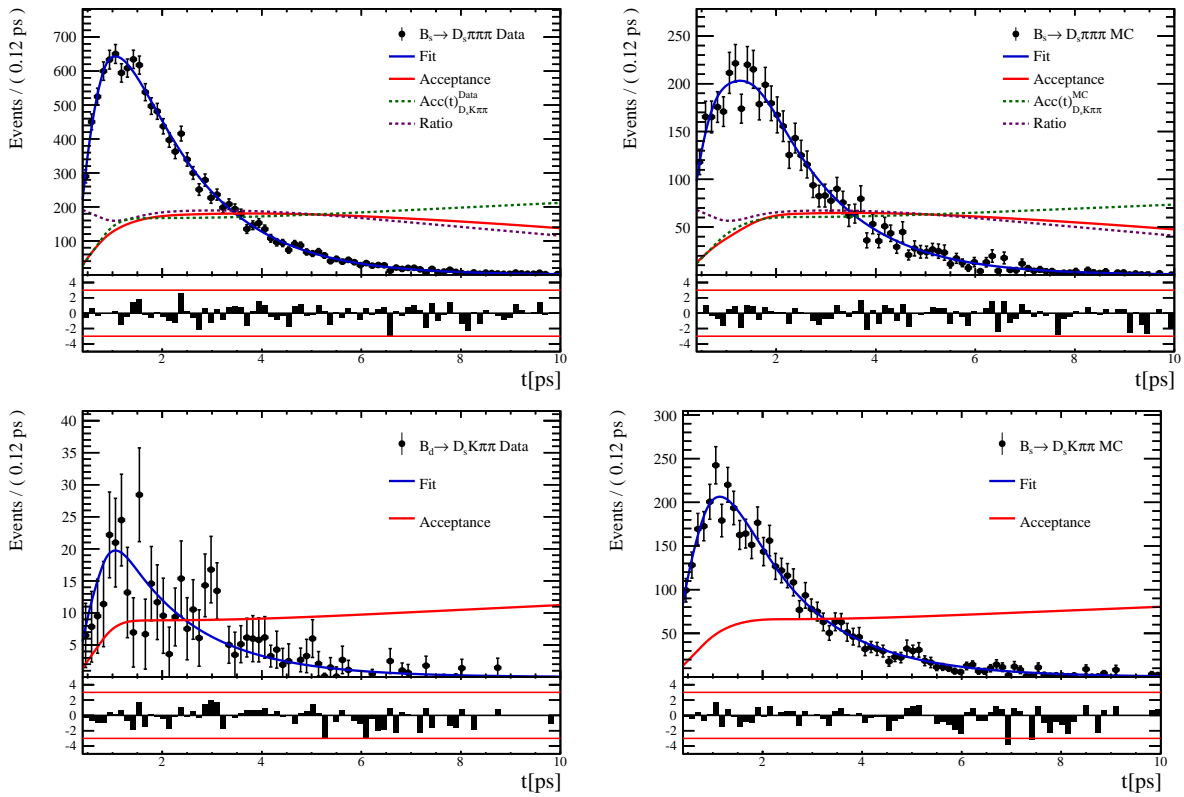


Figure 6.5

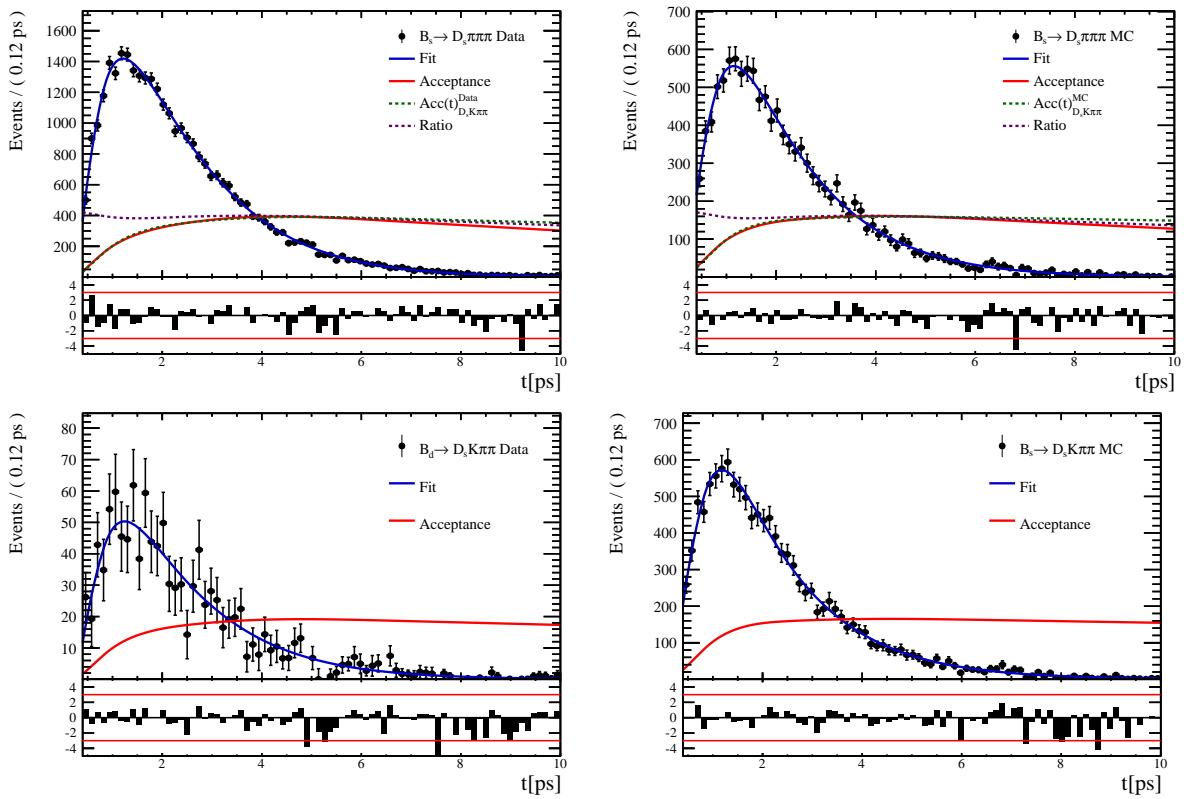


Figure 6.6

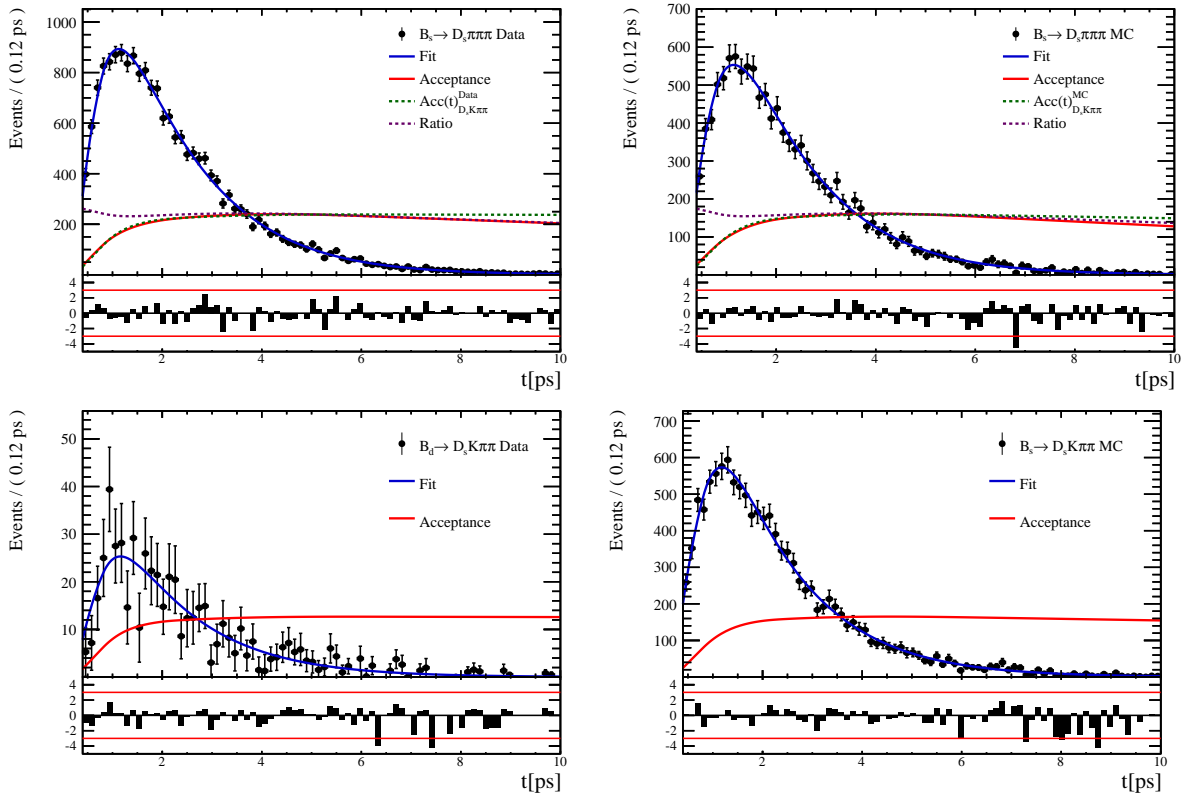


Figure 6.7

430 7 Decay-time Resoution

431 The observed oscillation of B mesons is prone to dilution, if the detector resolution is
432 of similar magnitude as the oscillation period. In the B_s^0 system, considering that the
433 measured oscillation frequency of the B_s^0 [8] and the average LHCb detector resolution [9]
434 are both $\mathcal{O}(50 \text{ fs}^{-1})$, this is the case. Therefore, it is crucial to correctly describe the
435 decay time resolution in order to avoid a bias on the measurement of time dependent CP
436 parameters.

437 In the presented analysis, we assume a gaussian resolution function with different
438 widths for each event. This gives rise to a per-event decay time error σ_t , which is
439 computed separately for every event along with the proper time t , by the decay time
440 fitter. Furthermore, the per-event decay time error σ_t is usually underestimated by the
441 decay time fitter, making it necessary to derive a scaling function, which matches the
442 per-event error to the actually measured decay time resolution.

443 Due to the lack of a decay time unbiased sample of real $B_s^0 \rightarrow D_s K \pi \pi$ decays, this
444 analysis relies on simulation to describe the time resolution. The obtained results will
445 be compared to those found in the closely related $B_s^0 \rightarrow D_s K$ analysis and systematic
446 uncertainties will be assigned conservatively. In the following, we investigate the Run1
447 and Run2 MC samples to find the proper decay time resolution in bins of the per-event
448 decay time errors and derive a scaling function from that.

450 7.1 Formalism

451 For simulated $B_s^0 \rightarrow D_s K \pi \pi$ events, the information on the true B_s^0 lifetime τ_{true} assigned
452 at production of the event, as well as the measured decay time $\tau_{measured}$, which is determined
453 after the interaction with the LHCb detector, is stored. In this analysis, the difference
454 $\Delta t = \tau_{true} - \tau_{measured}$ is obtained for each simulated $B_s^0 \rightarrow D_s K \pi \pi$ candidate. The width
455 of the distribution of Δt is a direct measure of the decay time resolution.

456 To analyse the relation between the per-event decay time error σ_t and the actual resolution,
457 the simulated sample is split into 8 bins of σ_t . Each bin width is chosen using an adaptive
458 binning scheme which ensures that approximately equal numbers of events are found
459 in every bin. A fit is then performed to the distribution of Δt in each of the bins to
460 determine the decay time resolution in the respective bin. After that, the correlation
461 between the binned per-event decay time error and the measured decay time resolution is
462 analyzed to determine the scaling function.

463 7.2 Decay-time Error in Run I & Run II

464 Due to the increase in center of mass energy from Run I to Run II, as well as (among
465 others) new tuning in the pattern and vertex reconstruction, the distributions of the raw
466 decay time error might not necessarily match each other between the two different runs.
467 Significant deviations can be observed in the shape and mean of those two distributions
468 for $B_s^0 \rightarrow D_s K \pi \pi$ signal candidates shown in Figure 7.1.

469 It can be observed that the decay time error distribution for signal candidates from Run
470 II is significantly broader and shifted to slightly higher values. Due to the discrepancies
471 between the distributions of the decay time error σ_r for Run I and Run II data, the time

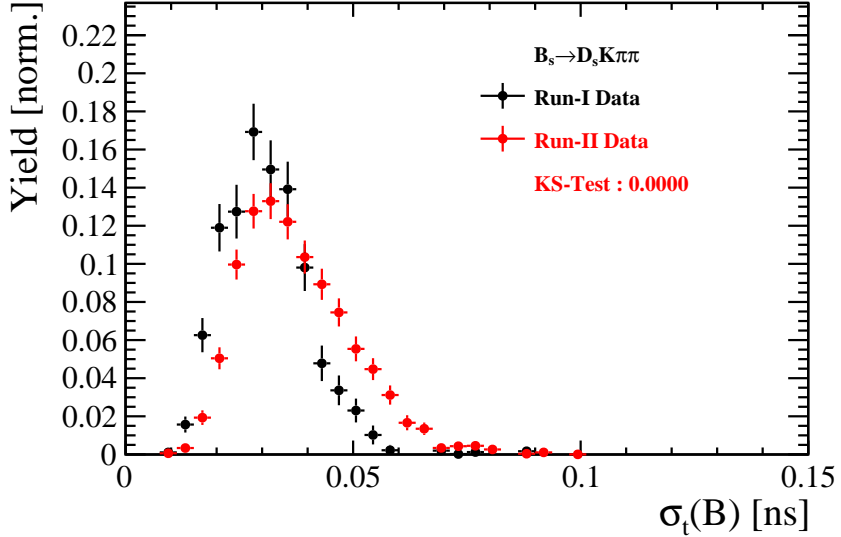


Figure 7.1: Distribution of the decay time error for $B_s^0 \rightarrow D_s K\pi\pi$ signal candidates on data for (black) Run I and (red) Run II. The signal distributions are obtained using the sWeight technique.

472 resolution studies have to be performed separately for both runs, which leads to two
473 different scaling functions to map $\sigma_t \rightarrow \sigma_{eff}$.

474 7.3 Fits to the decay time distributions

475 The sum of two Gaussian functions is used to fit the distributions of the decay time
476 difference Δt in each σ_t bin. One Gaussian function is relatively narrow and describes the
477 decay time of the majority of candidates in each bin, while the other, broader Gaussian
478 function describes candidates where the measured decay time differs considerably from
479 τ_{true} . Those contributions are shifted to the tails of the distribution. From the two
480 Gaussian functions, the combined, effective width σ_{eff} is quoted as decay time resolution
481 in each bin. Figure 7.2 shows the double Gaussian fit to the distribution of the decay time
482 difference for events where $20.7 \text{ ps} < \sigma_t < 24.3 \text{ ps}$. All fits are shown in the Appendix ???.
483

484 For the combination of the two separate widths σ_1 and σ_2 , a method which takes the
485 damping effect of the finite time resolution on the CP observables into account, is used.
486 The effective damping of the CP amplitudes is described by the dilution \mathcal{D} , which can
487 take values between 1 and 0. In the case of infinite precision, there would be no damping
488 and therefore $\mathcal{D} = 1$ would hold, while for a resolution that is much larger than the B_s^0
489 oscillation frequency, \mathcal{D} would approach 0. For two Gaussians describing the resolution,
490 the dilution can be defined as [?]

$$\mathcal{D} = f_1 e^{-\sigma_1^2 \Delta m_s^2 / 2} + (1 - f_1) e^{-\sigma_2^2 \Delta m_s^2 / 2}, \quad (7.1)$$

491 where f_1 is the fraction of events described by the first Gaussian relative to the second
492 and Δm_s is the oscillation period of the B_s^0 meson.

493 The dilution is computed in every bin of the per-event decay time error and can be
494 converted into the effective resolution

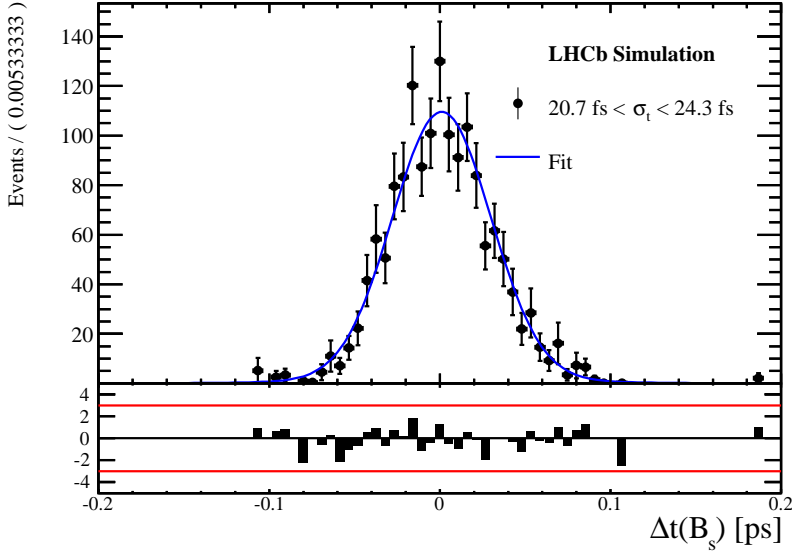


Figure 7.2: Difference of the true and measured decay time of $B_s^0 \rightarrow D_s K\pi\pi$ candidates from MC in the bin $20.7 \text{ ps} < \sigma_t < 24.3 \text{ ps}$. A fit of the sum of two Gaussian functions is overlaid.

$$\sigma_{eff} = \sqrt{(-2/\Delta m_s^2) \ln \mathcal{D}}. \quad (7.2)$$

495 7.4 Results

496 The fitted values for the Gaussian widths σ_1 and σ_2 , the fraction of the first relative to
 497 the second Gaussian function f_1 , as well as the effective resolution σ_{eff} , found in each bin
 498 σ_t , are shown in Tab. 7.1. Figure 7.3 shows the obtained values for σ_{eff} as a function of
 499 the per-event decay time error σ_t . A linear polynom of the form

$$\sigma(\sigma_t)_{mc} = s_0 + s_1 \cdot \sigma_t \quad (7.3)$$

500 is used to parametrise this distribution. The obtained values are

$$\sigma(\sigma_t)_{mc} = 0 + (1.257 \pm 0.017)\sigma_t, \quad (7.4)$$

501 where s_0 is compatible with 0 in the fit and therefore is set to $s_0 = \sigma(\sigma_t = 0) = 0$. For
 502 comparison, the linear scaling functions found for $\sigma(\sigma_t)$ in the $B_s^0 \rightarrow D_s K$ analysis [?] for
 503 MC is also shown in Figure 7.3. Motivated by the similarity between the $B_s^0 \rightarrow D_s K\pi\pi$
 504 and $B_s^0 \rightarrow D_s K$ decay, we assume a comparable scaling relation for data,

$$\frac{\sigma(t)_{D_s K\pi\pi, data}}{\sigma(t)_{D_s K\pi\pi, mc}} \approx \frac{\sigma(t)_{D_s K, data}}{\sigma(t)_{D_s K, mc}}. \quad (7.5)$$

505 This leads to a correction factor

$$\sigma(t)_{D_s K\pi\pi, data} \approx \frac{\sigma(t)_{D_s K, data}}{\sigma(t)_{D_s K, mc}} \cdot \sigma(t)_{D_s K\pi\pi, mc}, \quad (7.6)$$

506 where all elements of the right side of the equation are known.

507

508 Taking the scaling function found in our simulation, as well as input from the $B_s^0 \rightarrow$
 509 $D_s K$ analysis for $\sigma(t)_{D_s K, mc/data}$, we find

$$\sigma(t)_{D_s K \pi\pi, data} = 10.3 fs + 1.28 \cdot t$$

510 ,
 511 which is the scaling factor used for the per-event decay time error in the nominal time-
 512 and amplitude-dependent fit.

σ_t Bin [fs]	σ_1 [fs]	σ_2 [fs]	f_1	D	σ_{eff} [fs]
0to19	22.57 ± 0.96	45.57 ± 4.061	0.827 ± 0.057	0.89 ± 0.067	27.46 ± 8.82
19to24	24.64 ± 1.03	46.65 ± 3.109	0.768 ± 0.061	0.86 ± 0.070	30.64 ± 8.48
24to29	30.96 ± 0.90	58.76 ± 5.684	0.884 ± 0.045	0.83 ± 0.05	34.66 ± 5.28
29to34	35.28 ± 1.54	57 ± 6.698	0.839 ± 0.098	0.79 ± 0.10	39.09 ± 10.47
34to39	37.05 ± 2.36	61.98 ± 5.769	0.707 ± 0.12	0.73 ± 0.12	44.76 ± 11.78
39to44	68.38 ± 8.33	42.15 ± 3.583	0.331 ± 0.18	0.66 ± 0.16	50.98 ± 15.11
44to49	199.9 ± 100.1	53.72 ± 1.419	0.020 ± 0.014	0.62 ± 0.02	54.89 ± 1.60
49to150	68.75 ± 165.3	68.92 ± 4.603	0.001 ± 0.97	0.47 ± 0.65	68.92 ± 63.42

Table 7.1: Summary of the obtained parameters from the resolution fits described above.

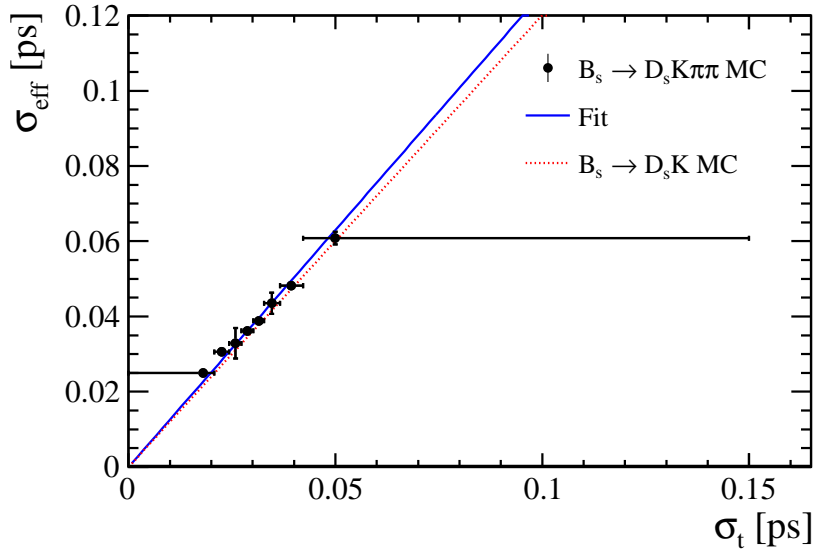


Figure 7.3: Decay-time resolution of $B_s^0 \rightarrow D_s K \pi\pi$ candidates from MC. The scaling functions found in $B_s^0 \rightarrow D_s K$ (dotted red line) MC is also shown for comparison. The fit described in the text is overlaid.

513 8 Time dependent fit

514 This section will cover the phasespace integrated, time dependent fit to $B_s^0 \rightarrow D_s h\pi\pi$ data,
 515 which is described by the PDF formulated in Eq. 2.6. For the phasespace integrated fit to
 516 $B_s^0 \rightarrow D_s K\pi\pi$ data, the sensitivity to the CKM phase γ will depend on the magnitude of
 517 the coherence factor κ , defined in Eq. 2.7, which is added as an additional fit parameter. In
 518 order to avoid any pollution of the final data samples by background events, both samples
 519 are weighted using the sWeights obtained by the fits to the invariant mass distributions,
 520 described in Sec. 4. This fit approach is commonly known as *sFit*. As additional input to
 521 the fit, the tagging information (Sec. 5), as well as the decay time acceptance (Sec. 6)
 522 and resolution (Sec. 7) is used and fixed to the values obtained by the dedicated studies.
 523 Taking all inputs into account, the final time dependent fit PDF is given by

$$\mathcal{P}\mathcal{D}\mathcal{F}(t, \vec{\lambda}) = \left(\epsilon(t) \cdot \int P(x, t, q_t, q_f) dx \right) \times \mathcal{R}(t - t'), \quad (8.1)$$

524 where $\int P(x, t, q_t, q_f) dx$ is the PDF given by Eq. 2.6, $\epsilon(t)$ is the efficiency due to the
 525 time acceptance effects and $\mathcal{R}(t - t')$ is the Gaussian time resolution function.

526 8.1 sFit to $B_s^0 \rightarrow D_s \pi\pi\pi$ data

527 The phasespace-integrated, time-dependent fit is performed to the full sWeighted sample
 528 of selected candidates from Run I and 2015+2016 Run II data, containing both possible
 529 magnet polarities and D_s final states. In the fit, the values of Γ_s and $\Delta\Gamma_s$ are fixed to the
 530 latest PDG report. All tagging parameters are fixed to the central values found in the
 531 tagging calibration, described in Sec. 5. Due to the fact that the $B_s^0 \rightarrow D_s \pi\pi\pi$ decay is
 532 flavour specific, the CP-coefficients can be fixed to $C = 1$ and $D_f = D_{\bar{f}} = S_f = S_{\bar{f}} = 0$,
 533 reducing Eq. 2.6 to

$$\int P(x, t, q_t, q_f) dx = [\cosh\left(\frac{\Delta\Gamma t}{2}\right) + q_t q_f C \cos(m_s t)] e^{-\Gamma t}. \quad (8.2)$$

534 Note that in this case, the dependence on the coherence factor κ is dropped and the
 535 same relation as found for $B_s^0 \rightarrow D_s \pi$ decays is recovered. Therefore, the only free fit
 536 parameter left is Δm_s . The data distribution with the overlaid fit is shown in Fig. xXx
 537 and the obtained value for the mixing frequency is

$$\Delta m_s = xx.xxx \pm 0.yyy. \quad (8.3)$$

538 8.2 sFit to $B_s^0 \rightarrow D_s K\pi\pi$ data

539 8.3 Results

540 A Detailed mass fits

541 In this section, all fits to the mass distribution of $B_s^0 \rightarrow D_s \pi\pi\pi$ and $B_s^0 \rightarrow D_s K\pi\pi$
 542 candidates are shown. The fits are performed simultaneously for every year of datataking
 543 (2011, 2012, 2015 and 2016) and the D_s decay ($D_s \rightarrow KK\pi$ non-resonant, $D_s \rightarrow \phi\pi$,
 544 $D_s \rightarrow K^*K$, or $D_s \rightarrow \pi\pi\pi$) through which the final state is reached.

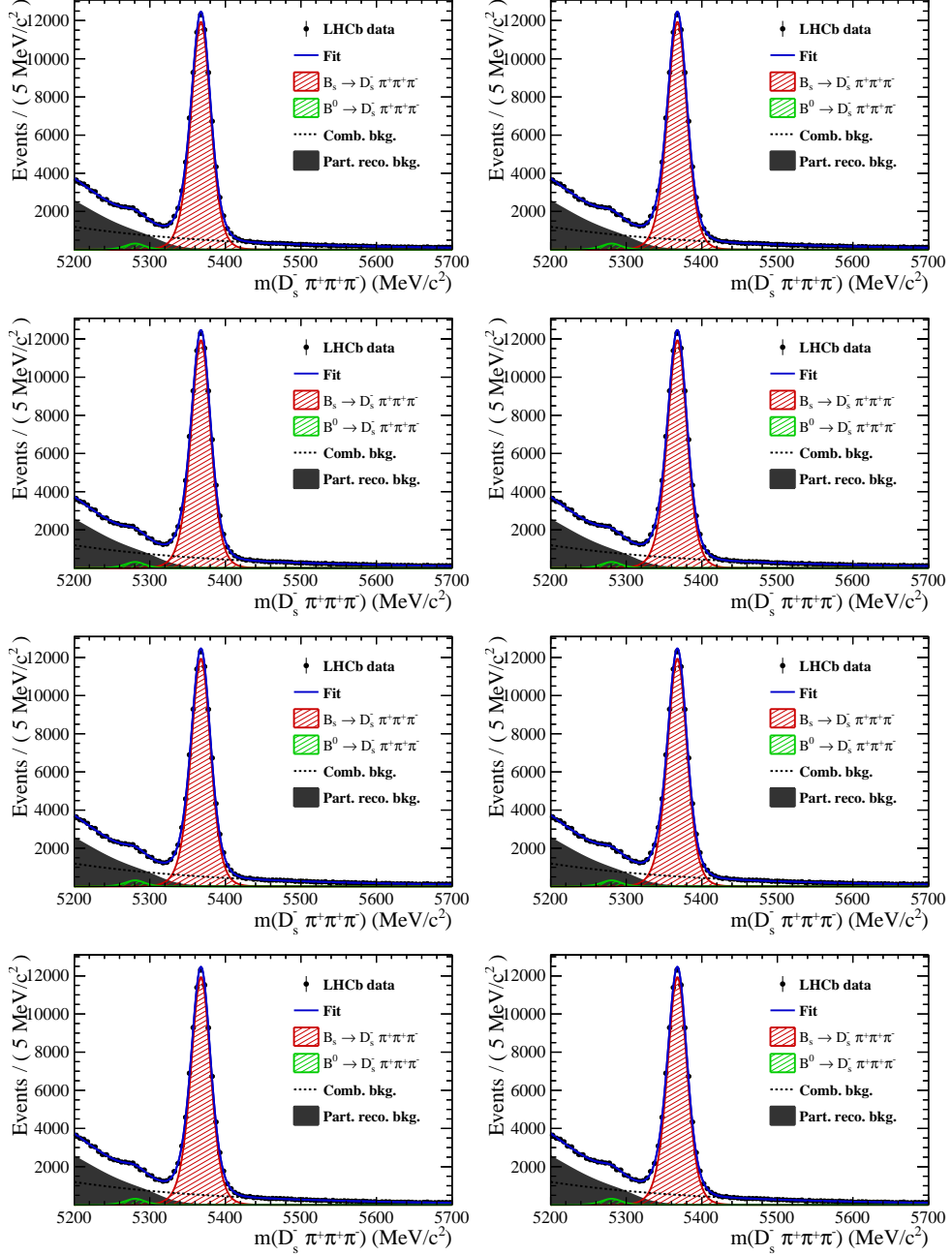


Figure 1.1: Invariant mass distributions of $B_s^0 \rightarrow D_s \pi\pi\pi$ candidates, ordered by D_s final state, for Run1 data. The fit described in 4.4 is overlaid.

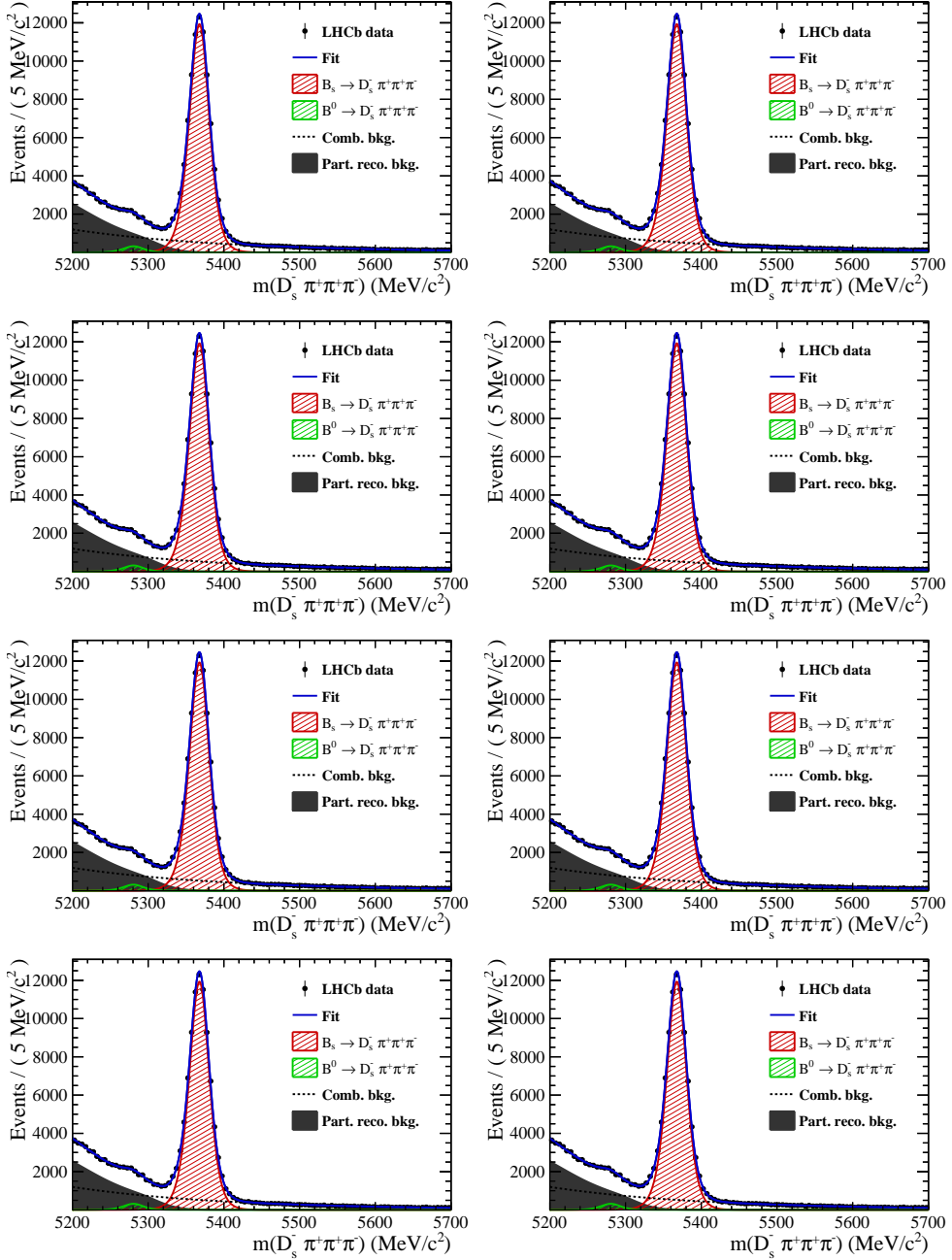


Figure 1.2: Invariant mass distributions of $B_s^0 \rightarrow D_s^- \pi^+ \pi^- \pi^+$ candidates, ordered by D_s final state, for Run2 data. The fit described in 4.4 is overlaid.

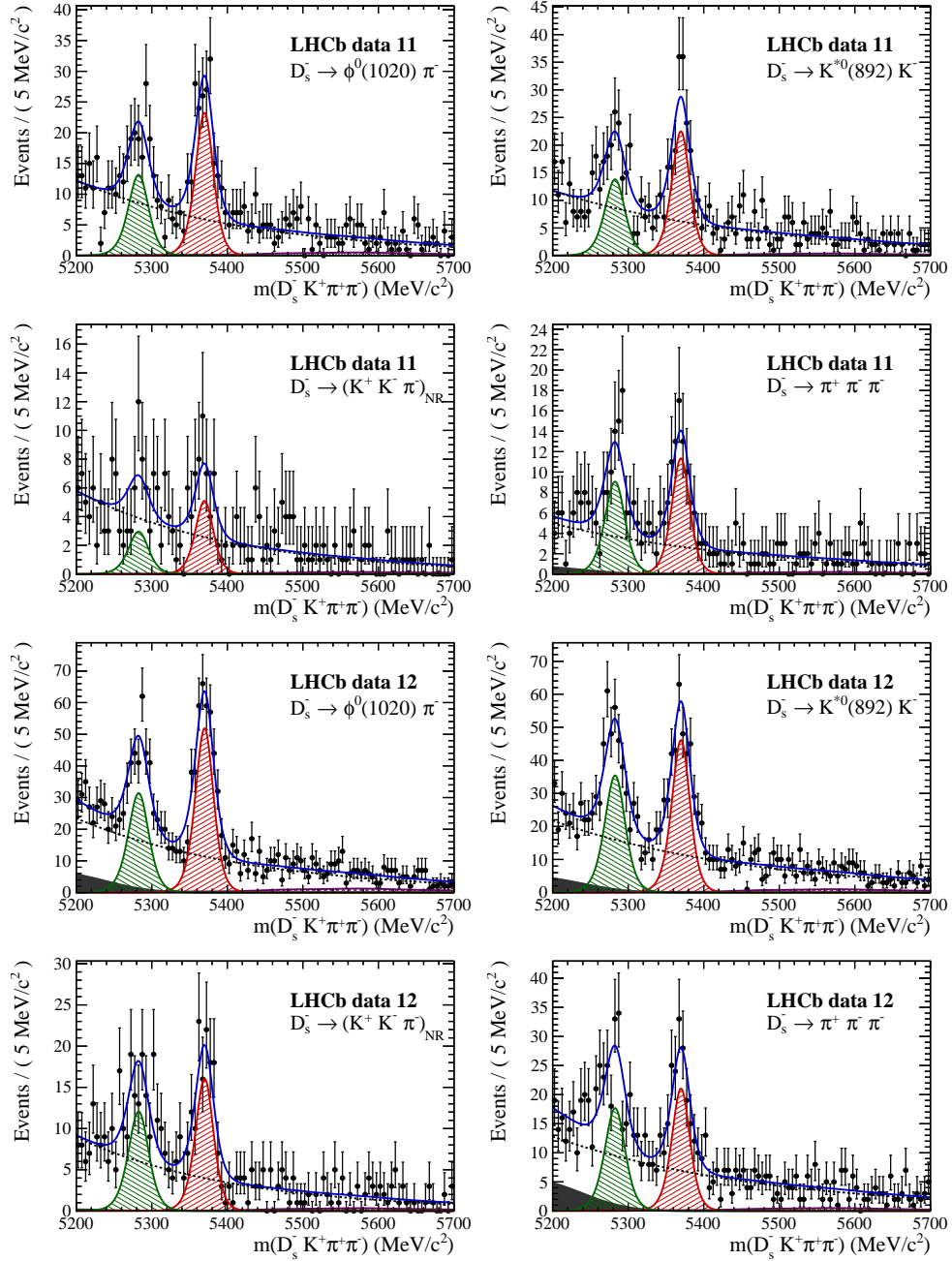


Figure 1.3: Invariant mass distributions of $B_s^0 \rightarrow D_s K\pi\pi$ candidates, ordered by D_s final state, for Run1 data. The fit described in 4.5 is overlaid.

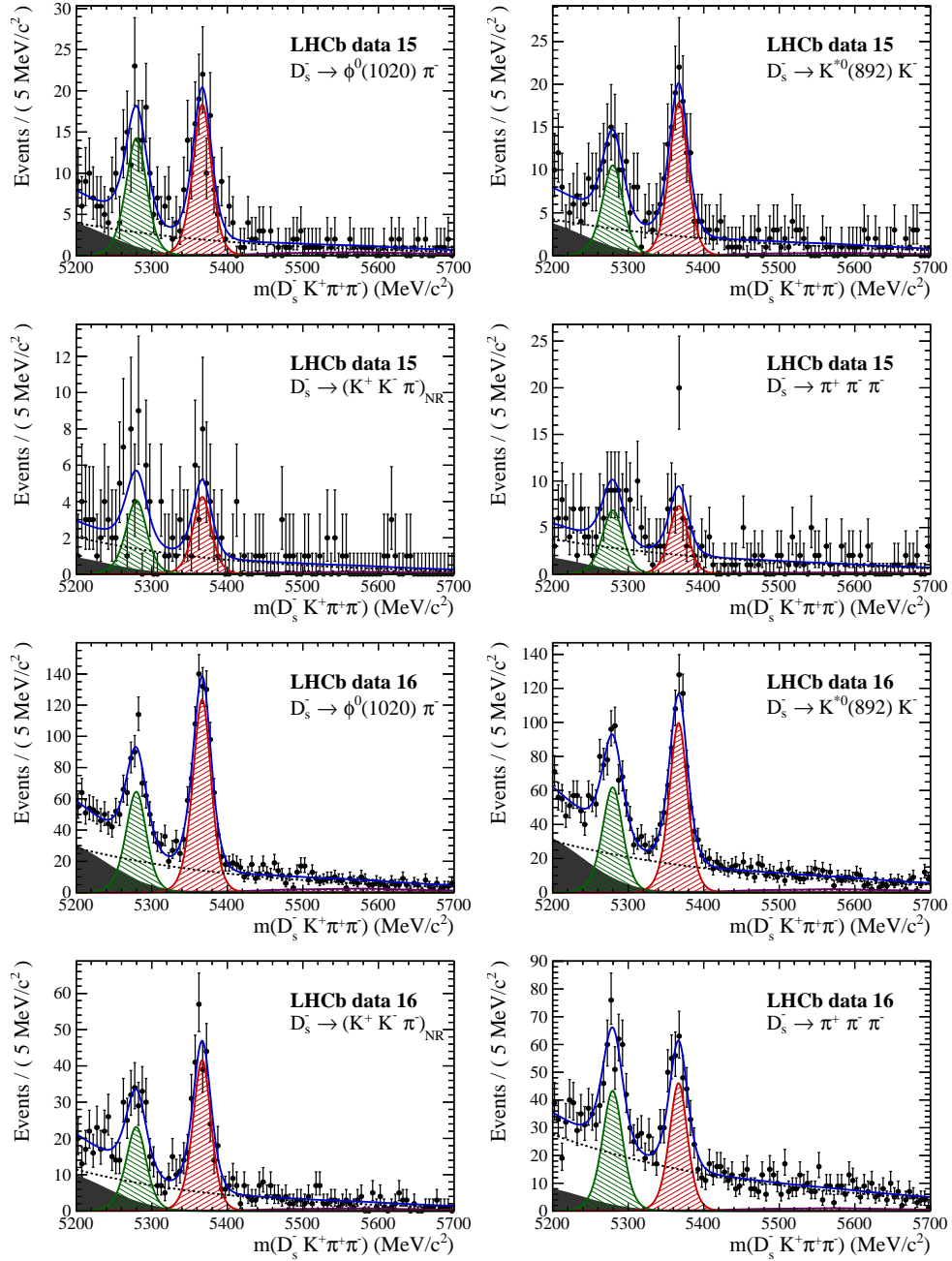


Figure 1.4: Invariant mass distributions of $B_s^0 \rightarrow D_s K \pi \pi$ candidates, ordered by D_s final state, for Ru2 data. The fit described in 4.5 is overlaid.

545 B Decay-time Resolution fits

546 This section contains all fits to the distributions of the decay time difference Δt between
 547 the true and the reconstructed decay time of the truth-matched B_s^0 candidates on MC.
 548 The fits are performed in bins of the decay time error σ_t , where an adaptive binning
 549 scheme is used to ensure that approximately the same number of events are found in each
 550 bin.

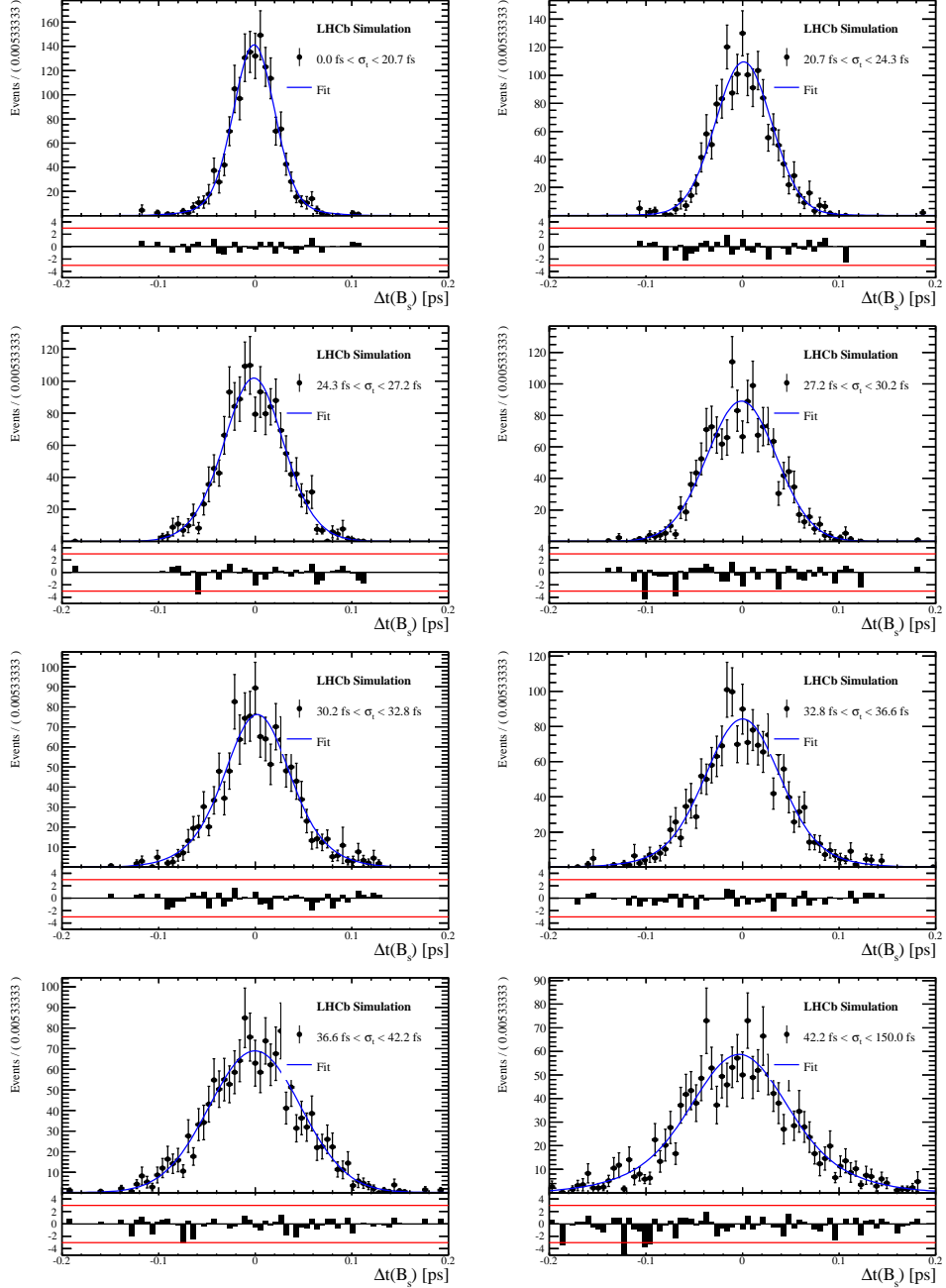


Figure 2.1: Difference of the true and measured decay time of $B_s^0 \rightarrow D_s K\pi\pi$ candidates from MC in all bins. The fit described in 7 is overlaid.

551 C MC corrections

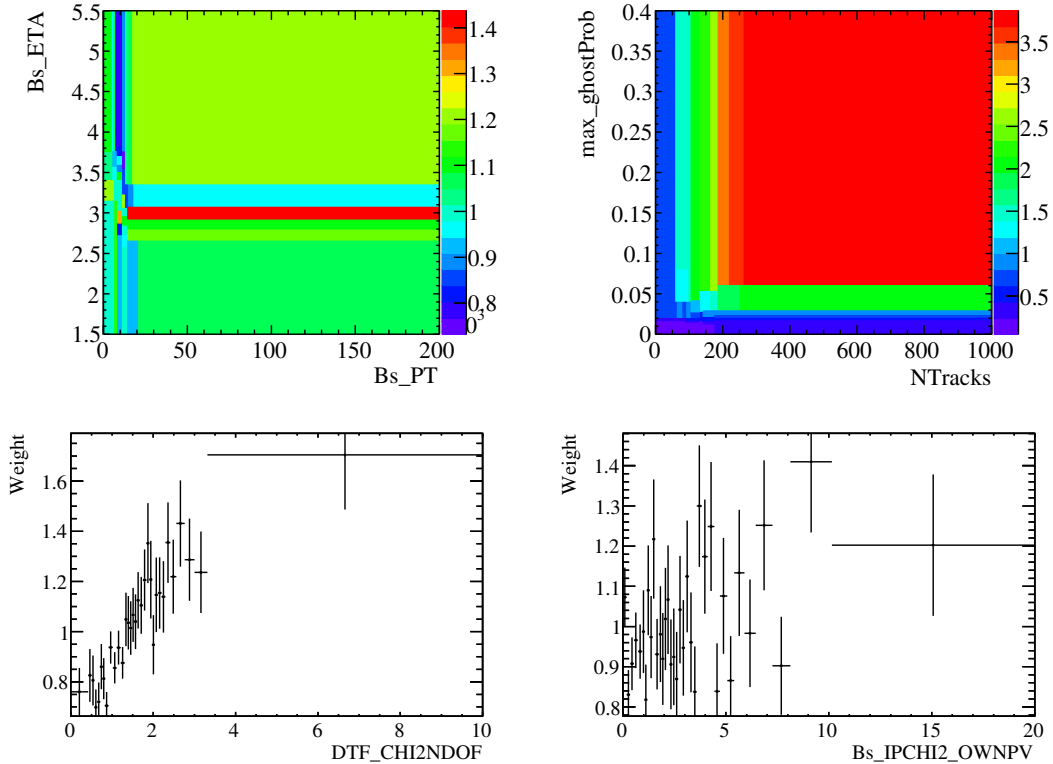


Figure 3.1: Weights applied to correct for Data/MC differences.

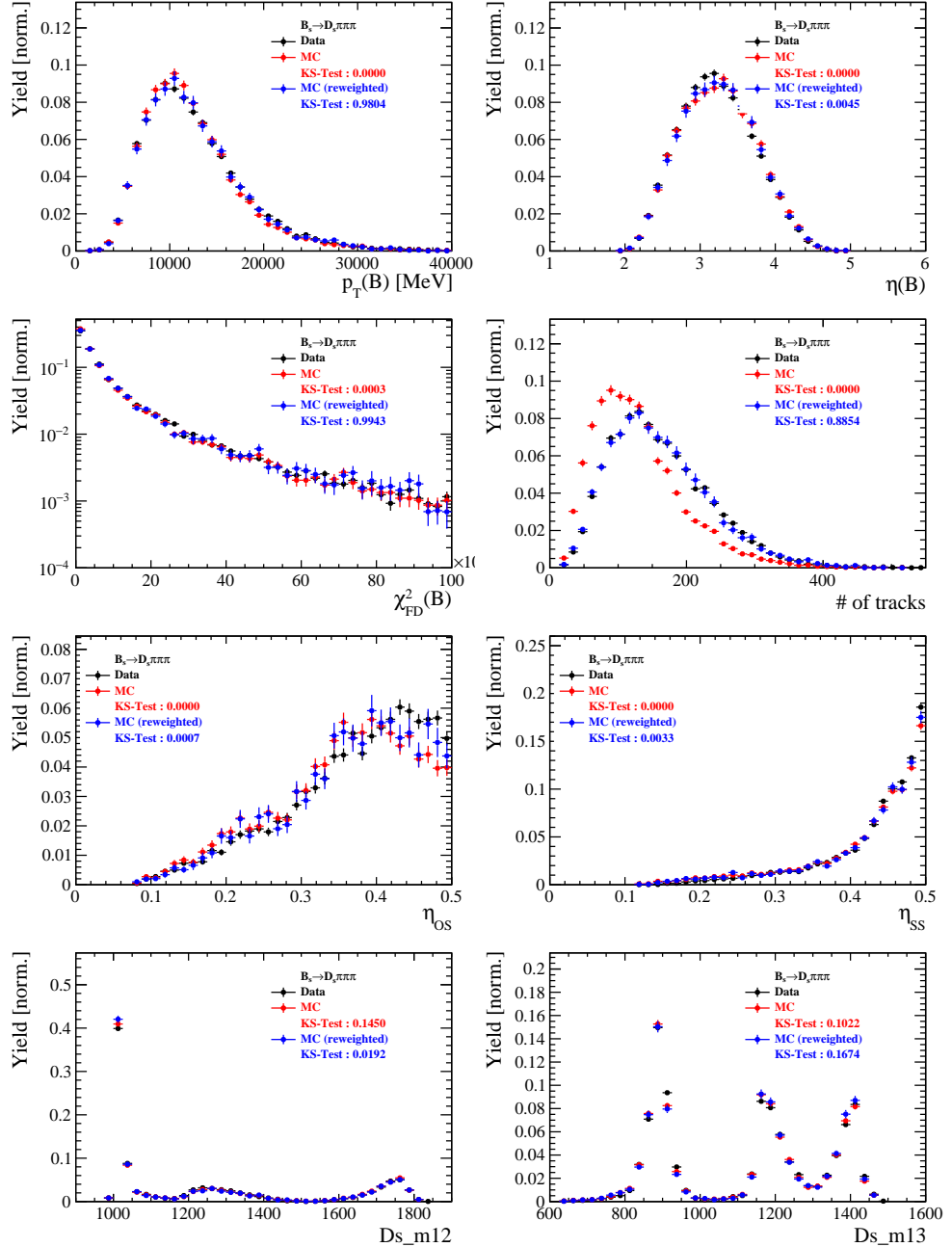


Figure 3.2: Comparison of selected variables for $B_s \rightarrow D_s \pi\pi\pi$ decays.

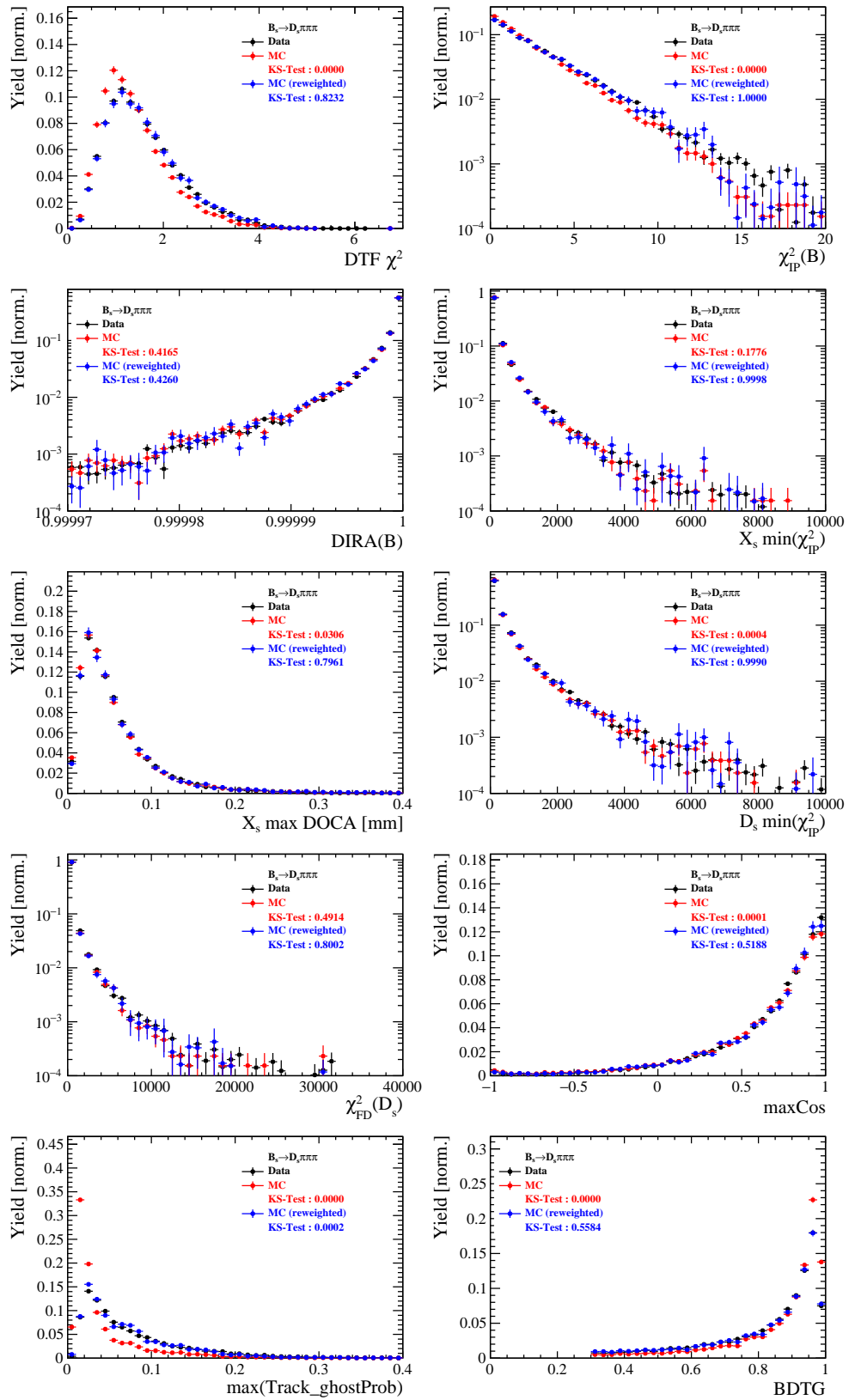


Figure 3.3: Comparison of BDTG input variables and classifier response for $B_s \rightarrow D_s \pi\pi\pi$ decays.

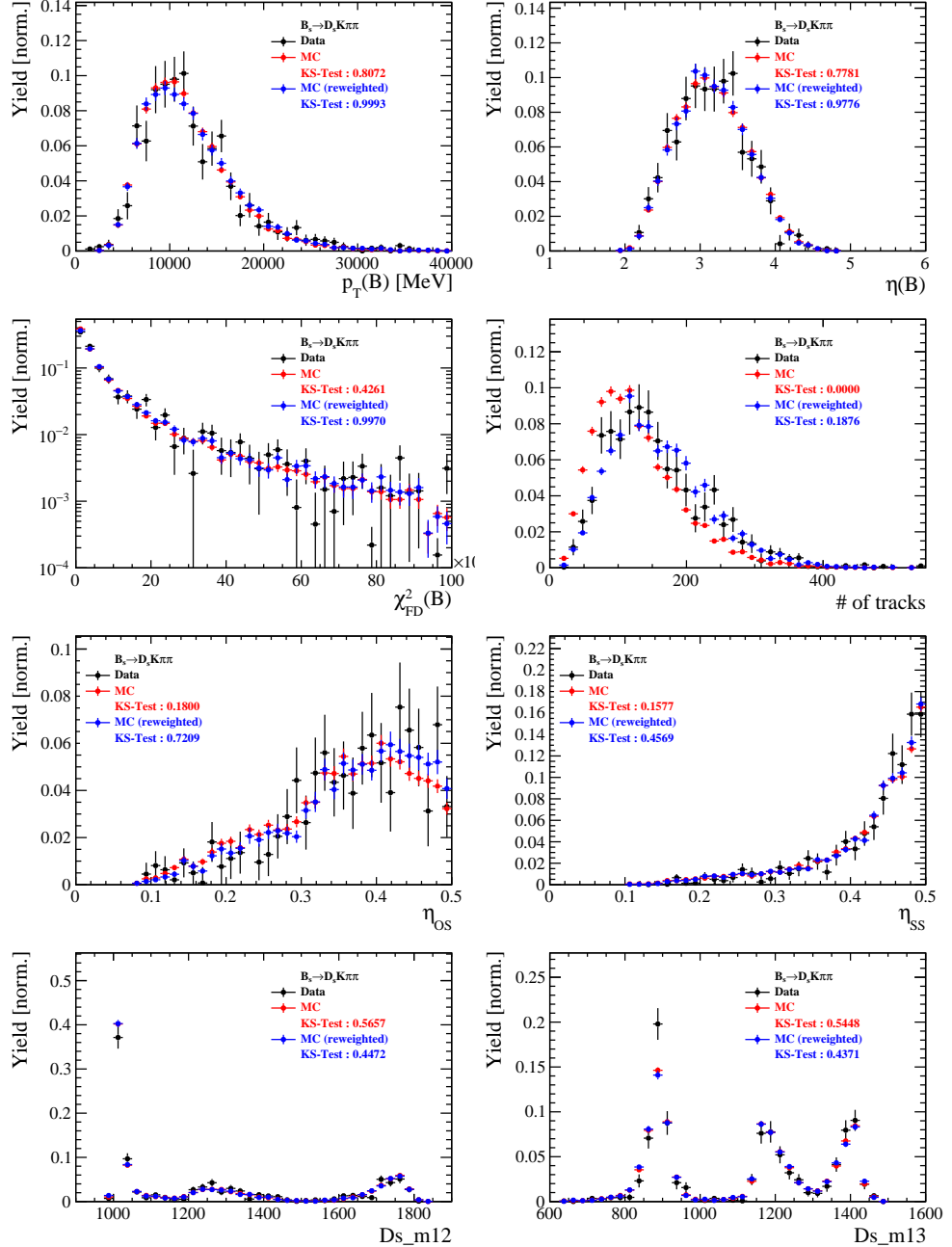


Figure 3.4: Comparison of selected variables for $B_s \rightarrow D_s K\pi\pi$ decays.

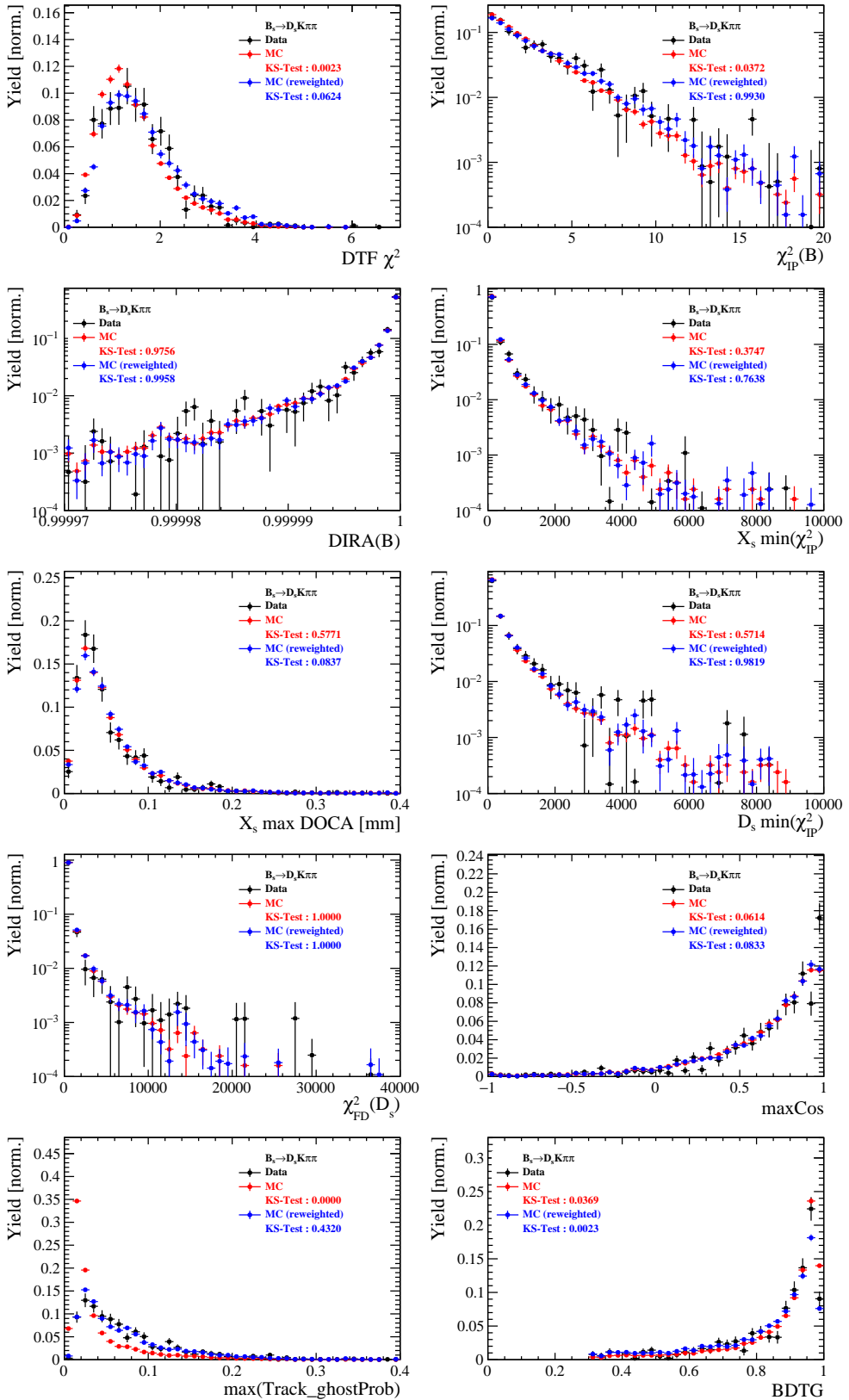


Figure 3.5: Comparison of BDTG input variables and classifier response for $B_s \rightarrow D_s K\pi\pi$ decays.

552 **D Data distributions**

553 **D.1 Comparison of signal and calibration channel**

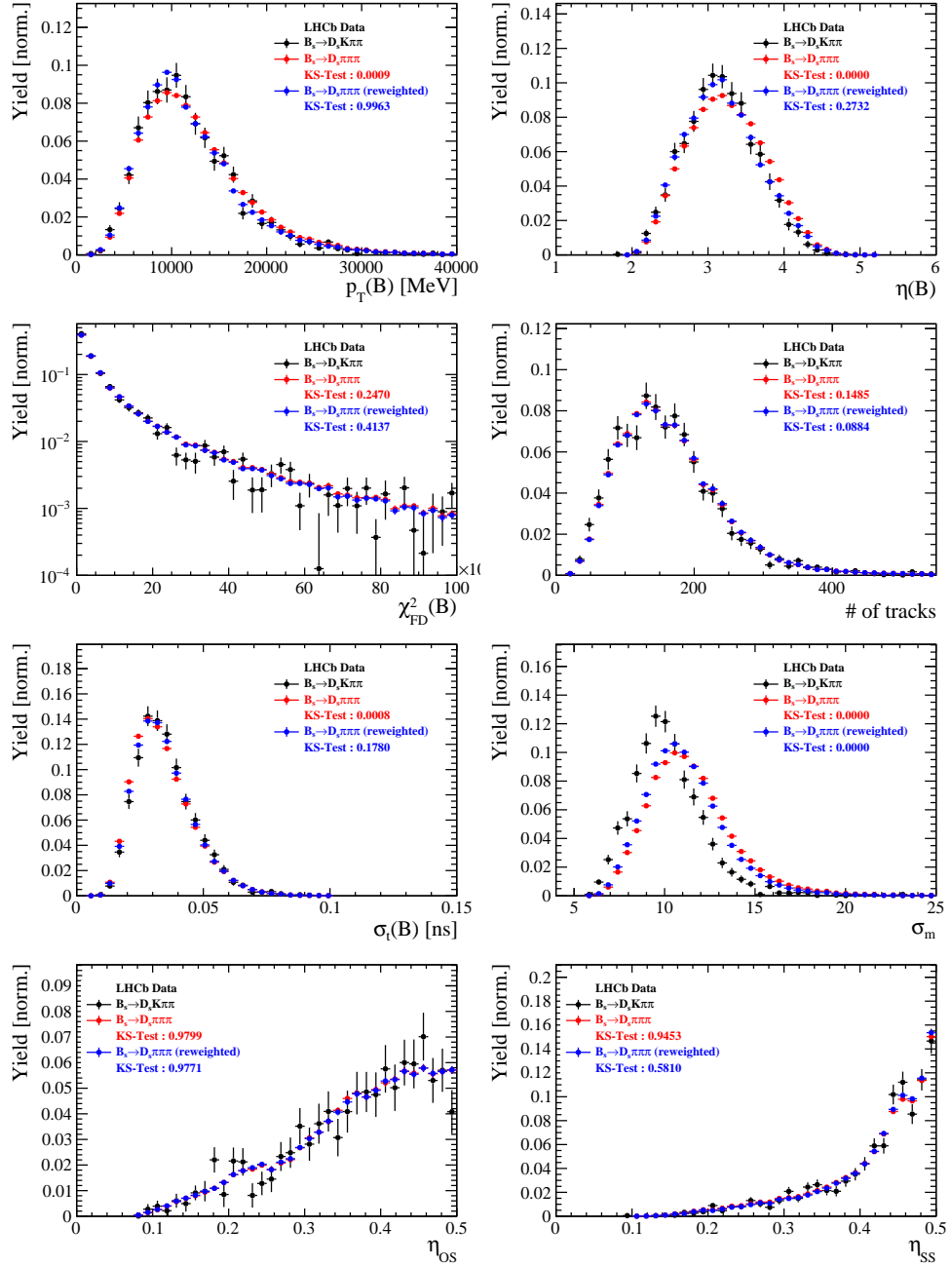


Figure 4.1: Comparison of selected variables.

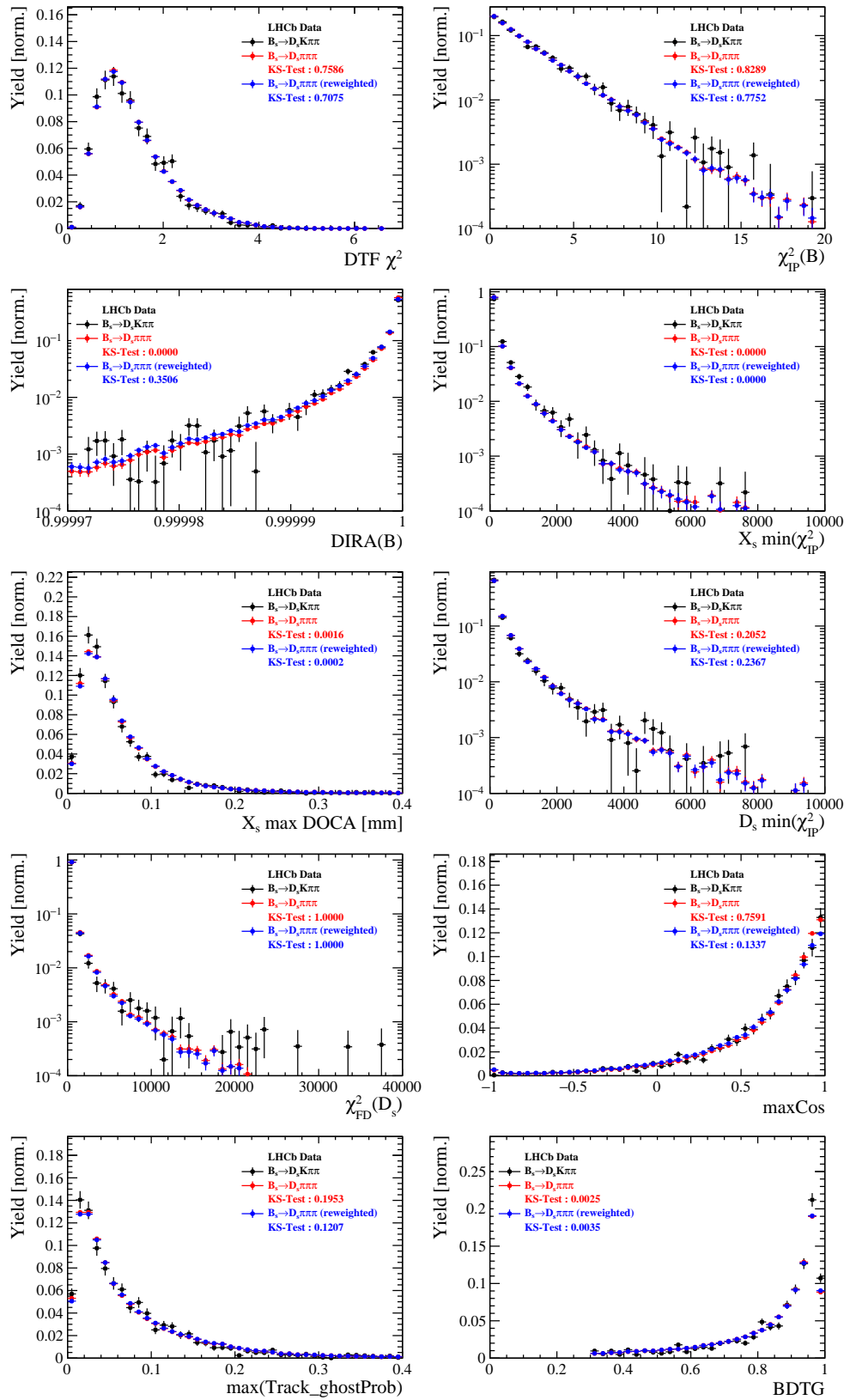


Figure 4.2: Comparison of BDTG input variables and classifier response.

554 D.2 Comparison of Run-I and Run-II data

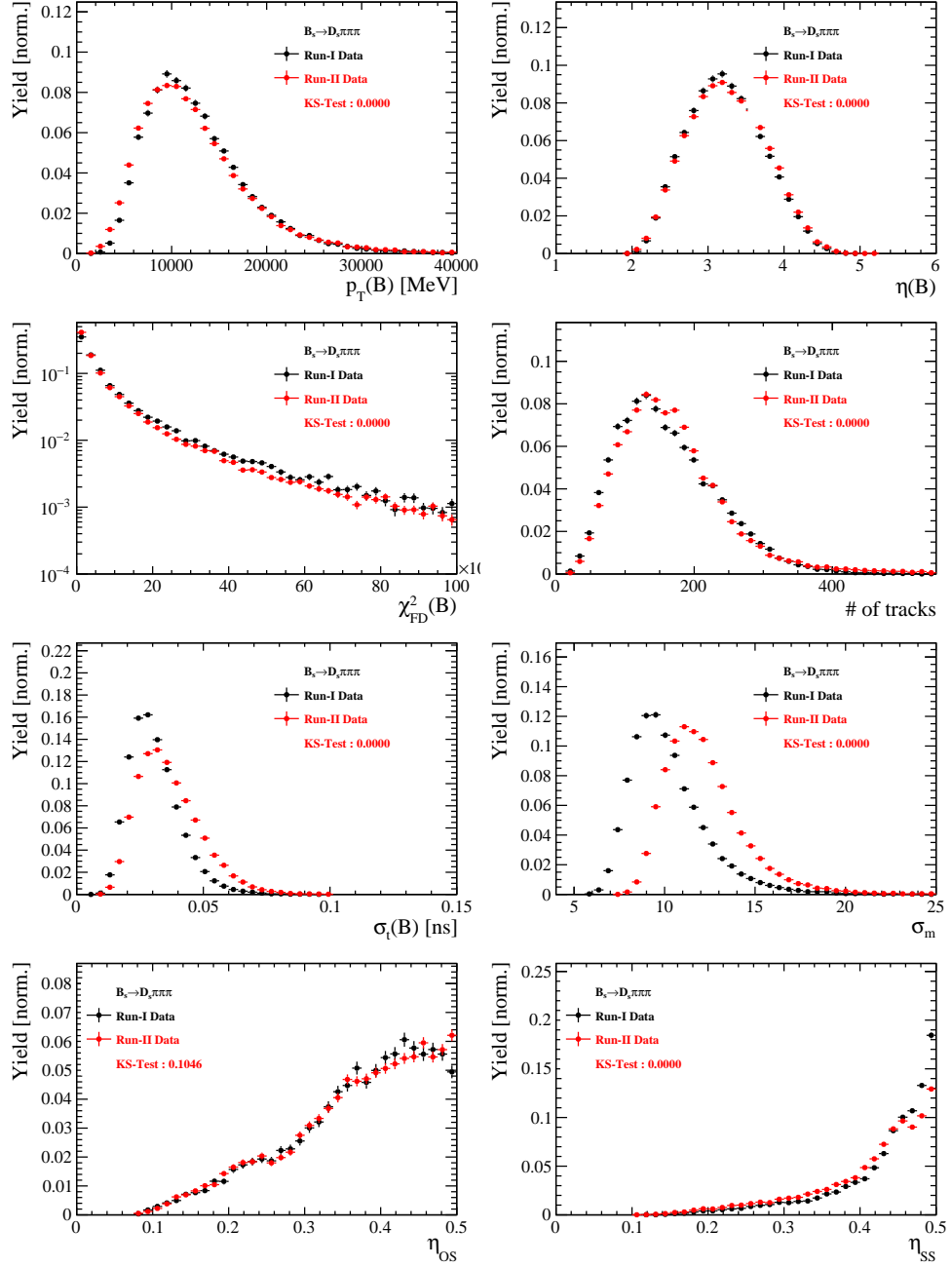


Figure 4.3: Comparison of selected variables.

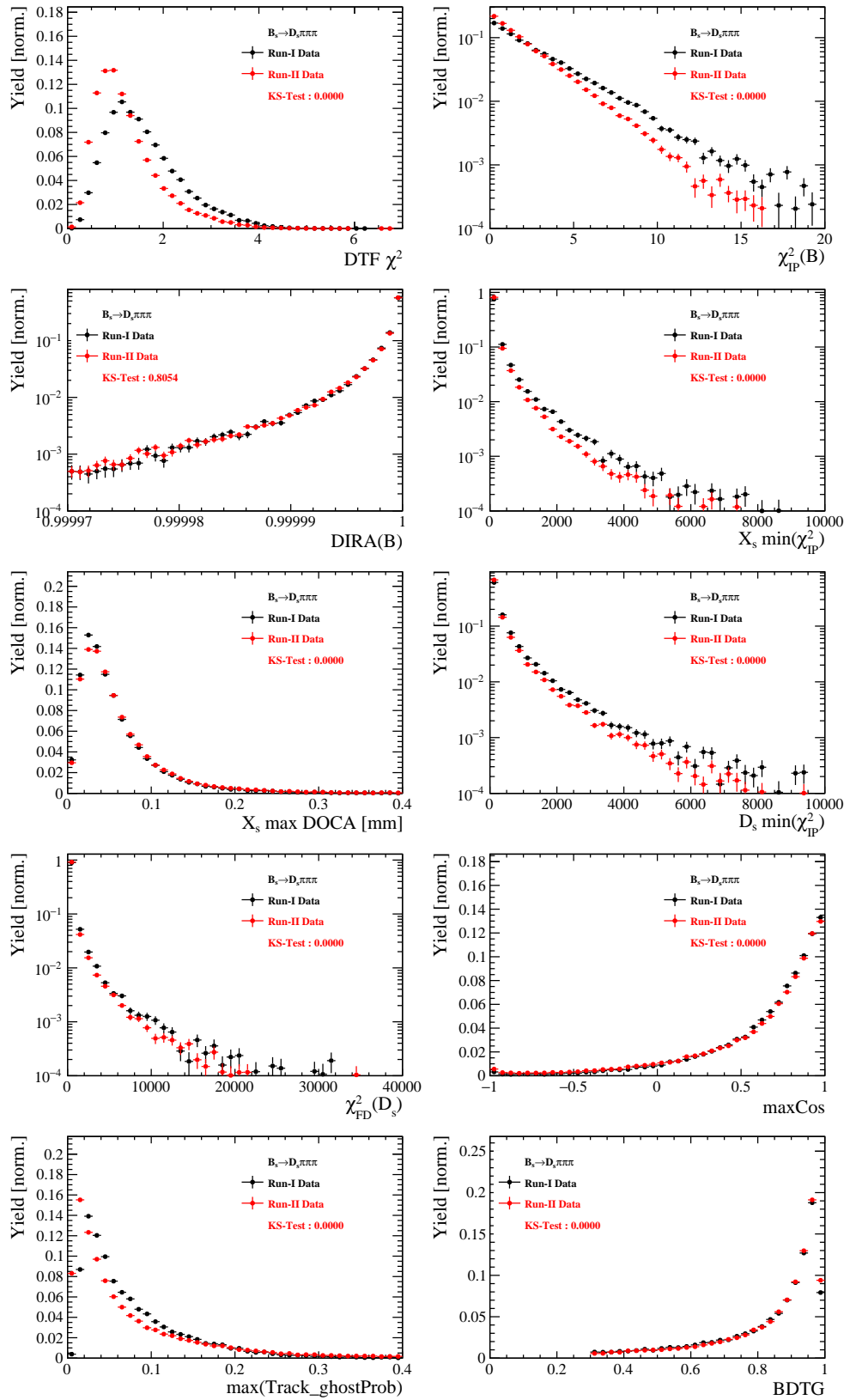


Figure 4.4: Comparison of BDTG input variables and classifier response.

555 D.3 Comparison of D_s final states

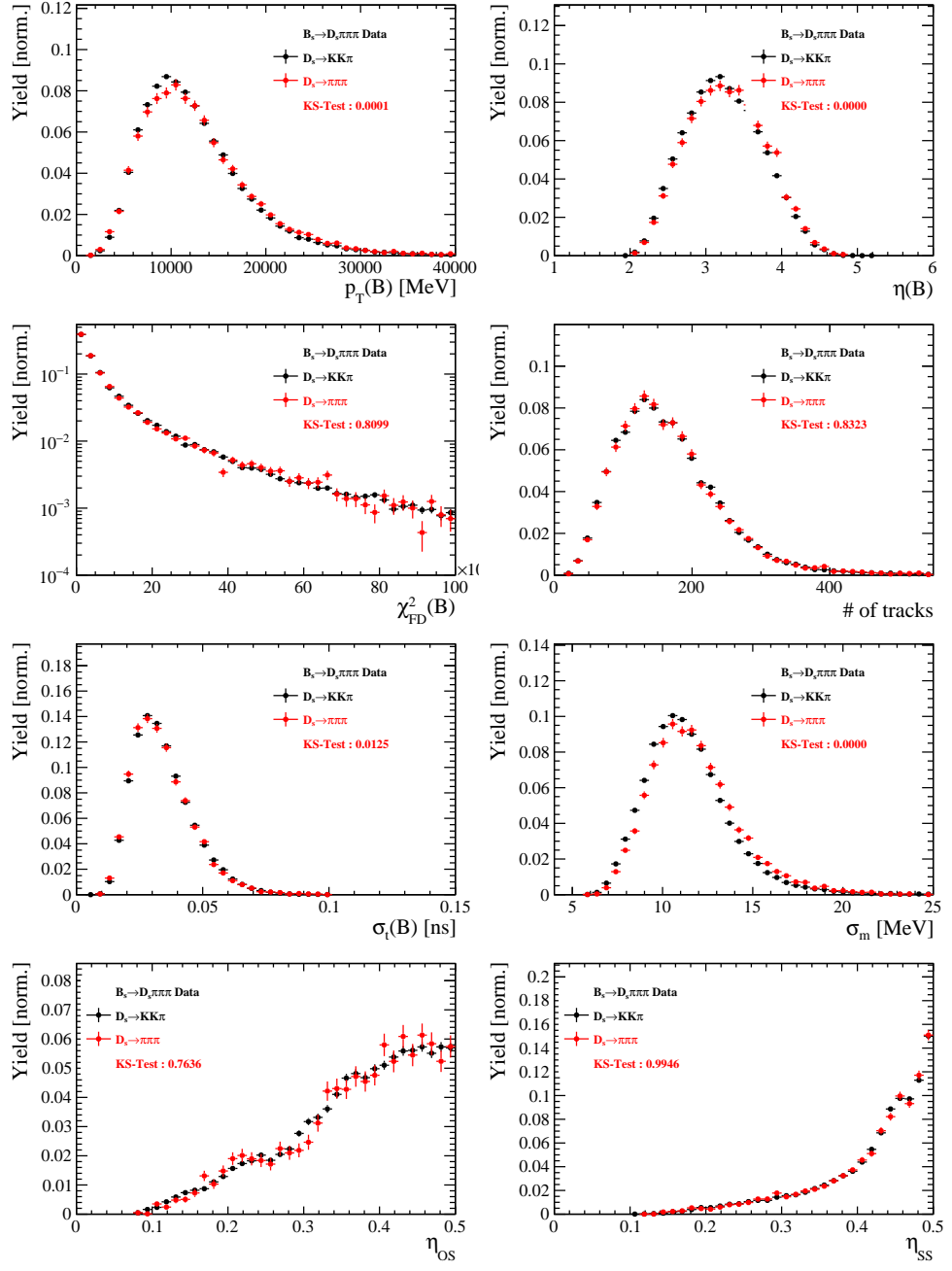


Figure 4.5: Comparison of selected variables.

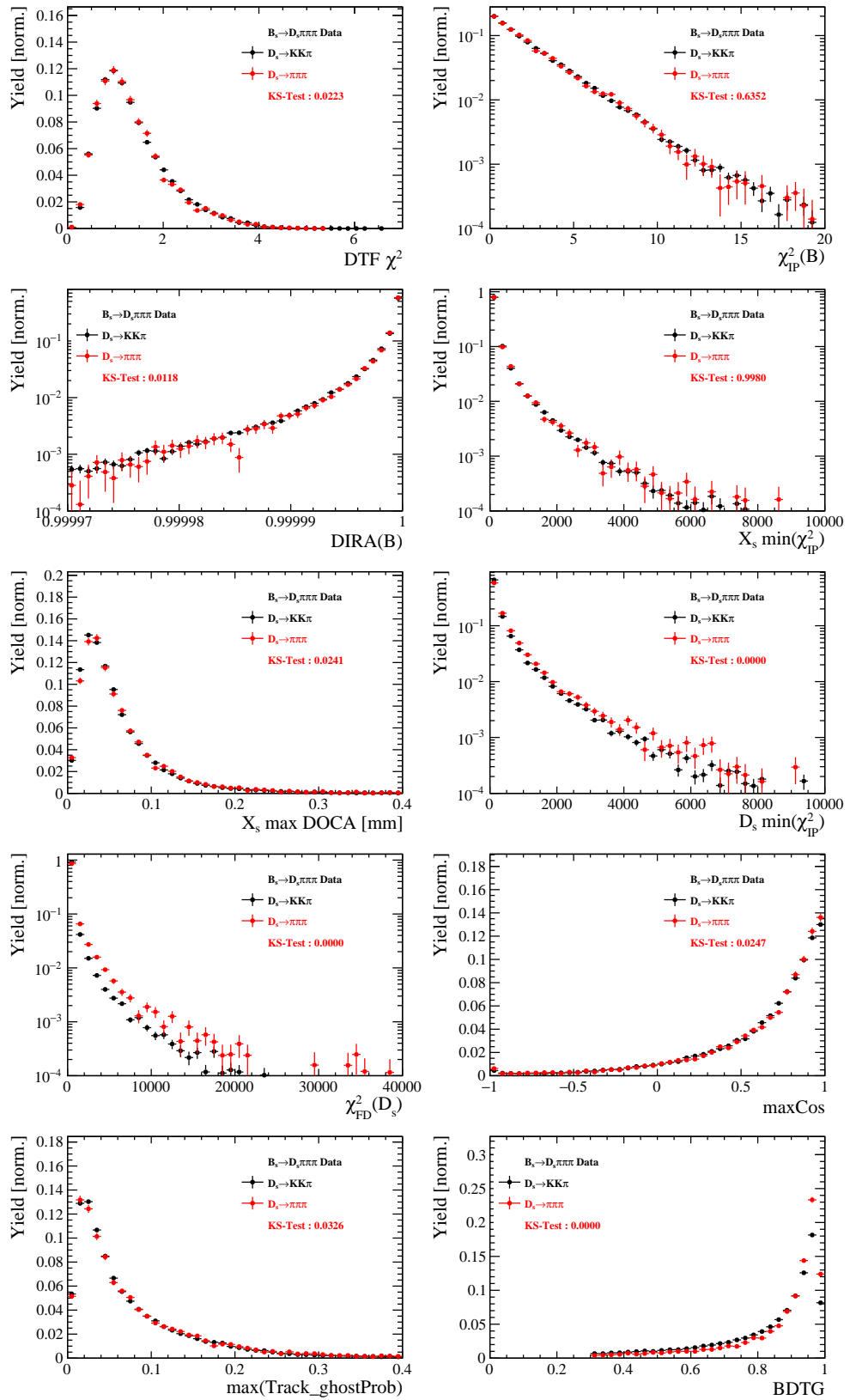


Figure 4.6: Comparison of BDTG input variables and classifier response.

556 D.4 Comparison of trigger categories

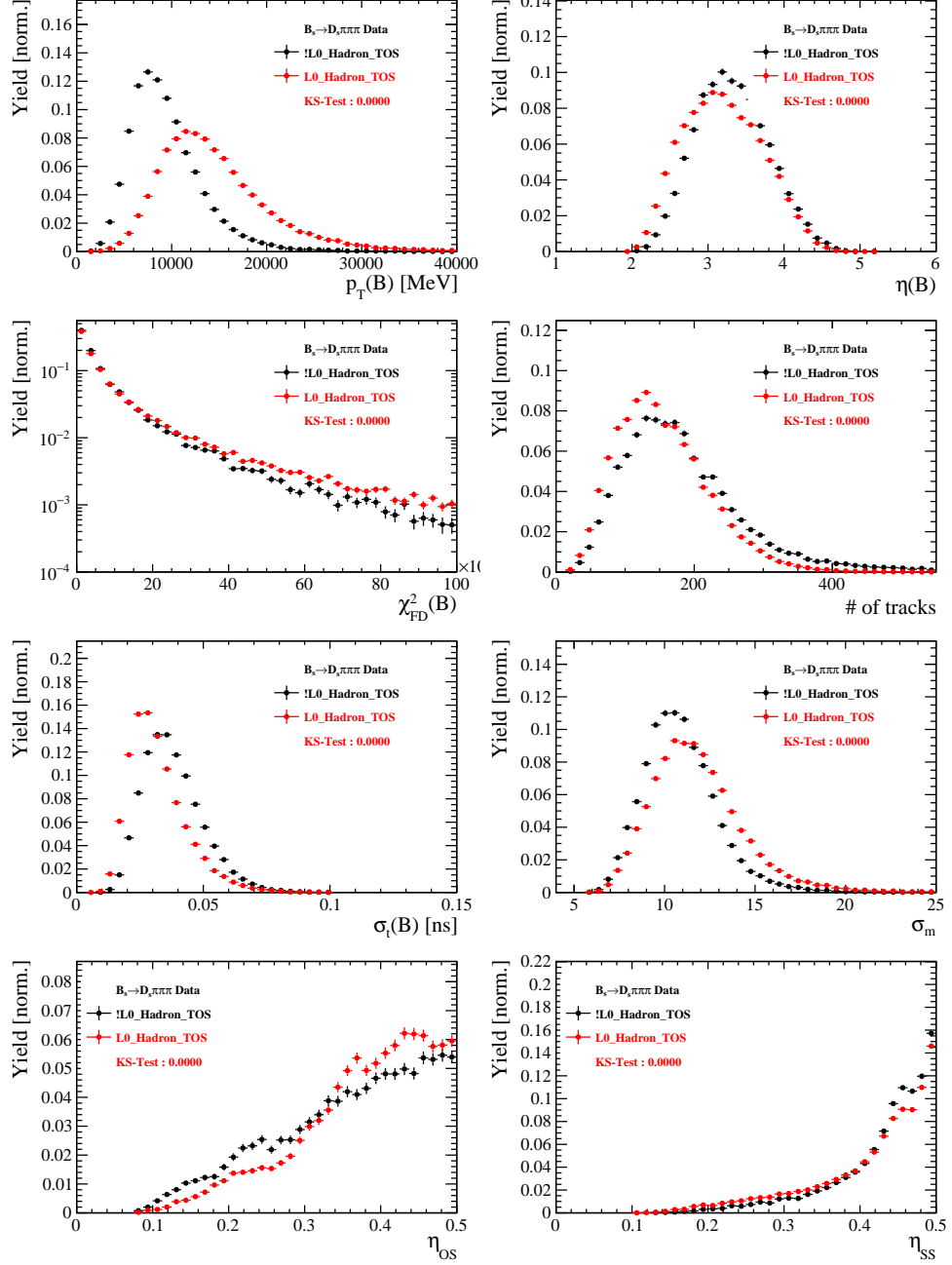


Figure 4.7: Comparison of selected variables.

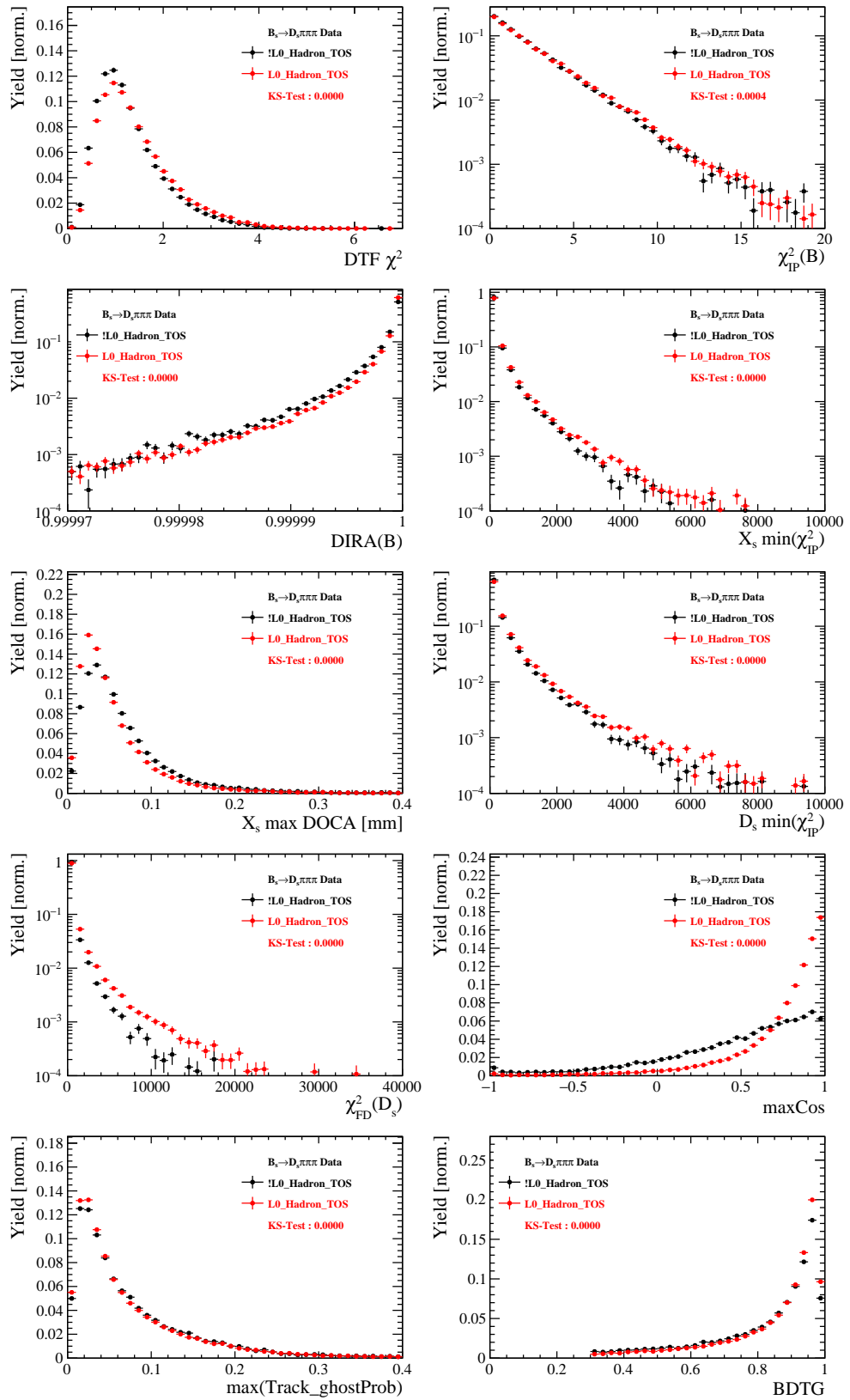


Figure 4.8: Comparison of BDTG input variables and classifier response.

557 **References**

- 558 [1] R. Fleischer, *New strategies to obtain insights into CP violation through $B(s) \rightarrow D(s) \rightarrow K^-$, $D(s)^* \rightarrow K^-$, ... and $B(d) \rightarrow D \rightarrow \pi^-$, $D^* \rightarrow \pi^-$, ... decays*, Nucl.
559 Phys. **B671** (2003) 459, arXiv:hep-ph/0304027.
- 560
- 561 [2] K. De Bruyn *et al.*, *Exploring $B_s \rightarrow D_s^{(*)\pm} K^\mp$ Decays in the Presence of a Sizable Width Difference $\Delta\Gamma_s$* , Nucl. Phys. **B868** (2013) 351, arXiv:1208.6463.
- 562
- 563 [3] S. Blusk, *First observations and measurements of the branching fractions for the decays $\bar{B}_s^0 \rightarrow D_s^+ K^- \pi^+ \pi^-$ and $\bar{B}^0 \rightarrow D_s^+ K^- \pi^+ \pi^-$* , .
564
- 565 [4] LHCb, S. Blusk, *Measurement of the CP observables in $\bar{B}_s^0 \rightarrow D_s^+ K^-$ and first observation of $\bar{B}_{(s)}^0 \rightarrow D_s^+ K^- \pi^+ \pi^-$ and $\bar{B}_s^0 \rightarrow D_{s1}(2536)^+ \pi^-$* , 2012. arXiv:1212.4180.
- 566
- 567 [5] A. Hoecker *et al.*, *TMVA: Toolkit for Multivariate Data Analysis*, PoS **ACAT** (2007) 040, arXiv:physics/0703039.
- 568
- 569 [6] Heavy Flavor Averaging Group, Y. Amhis *et al.*, *Averages of b-hadron, c-hadron, and τ -lepton properties as of summer 2014*, arXiv:1412.7515, updated results and plots
570 available at <http://www.slac.stanford.edu/xorg/hfag/>.
571
- 572 [7] T. M. Karbach, G. Raven, and M. Schiller, *Decay time integrals in neutral meson mixing and their efficient evaluation*, arXiv:1407.0748.
- 573
- 574 [8] Particle Data Group, K. A. Olive *et al.*, *Review of particle physics*, Chin. Phys. **C38**
575 (2014) 090001, and 2015 update.
- 576 [9] LHCb collaboration, R. Aaij *et al.*, *LHCb detector performance*, Int. J. Mod. Phys.
577 **A30** (2015) 1530022, arXiv:1412.6352.